Probing Intermolecular Interactions Involving Radicals with a Second Generation Energy Decomposition Analysis Using Absolutely Localized Molecular Orbitals

Yuezhi Mao,[*,†,‡] Daniel S. Levine,[†] Matthias Loipersberger,[†] Paul R. Horn,[†] and Martin Head-Gordon[*,†,¶]

† *Kenneth S. Pitzer Center for Theoretical Chemistry, Department of Chemistry, University of California at Berkeley, Berkeley, CA 94720, USA*

‡ *Present Address: Department of Chemistry, Stanford University, Stanford, CA 94305, USA*

¶ *Chemical Sciences Division, Lawrence Berkeley National Laboratory, Berkeley, CA 94720, USA*

E-mail: yuezhi.mao@berkeley.edu; mhg@cchem.berkeley.edu

Abstract

Intermolecular interactions between radicals and closed-shell molecules are ubiquitous in chemical processes, ranging from the benchtop to the atmosphere and extraterrestrial space. While energy decomposition analysis (EDA) schemes for closed-shell molecules can be generalized for studying radical-molecule interactions, they face challenges arising from the unique characteristics of the electronic structure of open-shell

species. In this work, we introduce additional steps that are necessary for the proper treatment of radical-molecule interactions to our previously developed unrestricted Absolutely Localized Molecular Orbital (uALMO)-EDA based on density functional theory calculations. A "polarize-then-depolarize" (PtD) scheme is used to remove arbitrariness in the definition of the frozen wavefunction, rendering the ALMO-EDA results independent of the orientation of the unpaired electron obtained from isolated fragment calculations. The contribution of radical rehybridization to polarization energies is evaluated. It is also valuable to monitor the wavefunction stability of each intermediate state, as well as their associated spin density profiles, to ensure the EDA results correspond to a desired electronic state. These radical extensions are incorporated into the "vertical" and "adiabatic" variants of uALMO-EDA for studies of energy changes and property shifts upon complexation. The EDA is validated on two model complexes, $H_2O\cdots{}^{\bullet}F$ and $FH\cdots{}^{\bullet}OH$. It is then applied to several chemically interesting radical-molecule complexes, including the sandwiched and T-shaped benzene dimer radical cation, complexes of pyridine with benzene and naphthalene radical cations, binary and ternary complexes of the hydroxyl radical with water ($^{\bullet}OH(H_2O)$ and $^{\bullet}OH(H_2O)_2$), and the pre-reactive complexes and transition states in the $^{\bullet}OH$ + HCHO and $^{\bullet}OH$ + CH_3CHO reactions. These examples suggest that this second generation uALMO-EDA is a useful tool for furthering one's understanding of both energetic and property changes associated with radical-molecule interactions.

1 Introduction

Understanding intermolecular interactions involving radicals is of key importance in many areas of chemical research. The uptake of radicals by closed-shell molecules gives rise to the pre- or post-reactive complexes in many atmospheric chemical reactions,[1–4] and the participation of neutral molecules (such as H_2O) can make a significant difference to reaction kinetics by modulating the relative stability of transition states or reaction intermediates.[5–11] In environments that facilitate ionization such as the interstellar medium, the interaction of radical cations with neutral molecules initiates many exotic clustering and even polymerization processes that are rarely observed under laboratory condition.[12–15] In addition, in organic reactions catalyzed by transition metal complexes, the association of a substrate with an open-shell metal center can be viewed as radical-molecule interaction as well. Compared to interactions between closed-shell molecules, radical-molecule interactions display unique characteristics. For example, a radical can behave as either an electron donor or acceptor, resulting in the formation of 2c-1e or 2c-3e bonds.[16,17] Moreover, a radical may have multiple closely lying electronic states, and their relative stability can be altered in the presence of other molecules.[18–21] The fundamental role played by these interactions in a wide range of chemical processes and their intriguing features have thus motivated the development of many theoretical methods aiming to further understand them.

Energy decomposition analysis (EDA)[22–25] is a category of methods that is able to separate the total intermolecular interaction energy into physically intuitive, meaningful terms, such as permanent electrostatics, polarization, dispersion, etc. While many perturbative or variational EDA schemes have been developed primarily for studying interactions between closed-shell molecules, not all of them have been extended to treat open-shell systems. Under the framework of symmetry-adapted perturbation theory (SAPT),[26,27] the open-shell equations have been derived for the SAPT0 level of theory (second order for intermolecular

correlation and zeroth order for intramolecular correlation),[28,29] and an efficient implementation using density fitting based on unrestricted Hartree-Fock (UHF) reference was reported recently.[30] EDA methods based on density functional theory (DFT) calculations commonly adopt the "supermolecular" approach, i.e., decomposing the total interaction energy defined as the difference between the energy of the full system and the sum of fragment energies. It is thus relatively straightforward to enable the application of these methods to open-shell systems by using unrestricted (U) or restricted open-shell (RO) self-consistent field (SCF) calculations at the fragment and supersystem levels. Such extensions have been achieved for the pair interaction (PI)-EDA,[31] the constrained space orbital variation (CSOV) approach,[32] and many other popular EDA schemes.[33–37] Besides DFT-based approaches, extensions of wavefunction theory (WFT)-based EDA schemes to open-shell systems have also been achieved, including the recently developed local energy decomposition (LED) analysis under the quasi-restricted[38] domain-based local pair natural orbital (DLPNO) framework[21] and the extension of absolutely localized molecular orbital (ALMO)-EDA to restricted open-shell second-order Møller-Plesset perturbation theory (ROMP2)[39] by some of us.[40]

In this paper, we present the recent development and applications of ALMO-EDA for studying radical-molecule interactions, i.e., the interactions between open-shell and closed-shell species. The original ALMO-EDA scheme partitions a total interaction energy into frozen interaction (FRZ), polarization (POL), and charge-transfer (CT) contributions,[41] and it was extended to treat systems involving radicals by Horn et al.[35] Recent years have seen the development of an improved, second-generation ALMO-EDA scheme,[42] which has addressed two limitations of the original approach: (i) the use of fragment electrical response functions (FERFs)[43] allows for a useful basis set limit for the separation of POL and CT contributions; (ii) the further decomposition of the FRZ term into contributions from permanent electrostatics (ELEC), Pauli repulsion (PAULI), and dispersion (DISP) was enabled.[44,45] Parallel to the development of ALMO-EDA for energetics, recently we also proposed the *adiabatic*

ALMO-EDA scheme to analyze changes in molecular properties induced by intermolecular binding.[46] This approach has shown its usefulness via applications in characterizing the origin of structural changes and/or vibrational frequency shifts upon the formation of hydrogen-bonding (HB),[46–48] halogen-bonding (XB),[20,49] and metal-carbonyl complexes.[50–52] In the following sections, we will focus on the applications of second-generation ALMO-EDA and the adiabatic ALMO-EDA to intermolecular interactions involving open-shell species. Other notable recent advances in ALMO-EDA include the extensions for treating bonded interactions[53,54] and interactions involving excited electronic states,[55,56] as well as developments for the use of correlated wavefunction methods.[40,57,58]

The initial supersystem state in the ALMO-EDA procedure, the frozen wavefunction, is typically constructed via a concatenation of fragment orbitals that are optimized in isolation.[41] The same choice was made by many other popular supermolecular approaches, such as the EDA-NOCV (natural orbitals for chemical valence) method[24,59,60] and the block-localized wavefunction (BLW)-EDA.[61–63] Even in SAPT,[26] the zeroth-order wavefunction is also chosen to be the direct product of unperturbed fragment wavefunctions. One challenge faced by all these methods in practice is that the initial state will *not* be uniquely defined when the open-shell species has degenerate electronic configurations. This is typically the case for radicals with highly symmetric structures, such as $F^\bullet$ (spherically symmetric) and $^\bullet OH$ ($C_{\infty v}$).

We demonstrate this problem using the $H_2O\cdots F^\bullet$ complex from the dataset of radical-neutral complexes by Tentscher and Arey (referred to as the TA13 dataset throughout this paper),[64] whose geometry is shown in Fig. 1(a). As shown in the leftmost two panels of Fig. 2, when $F\cdots O$ is along the z axis ("z-aligned"), the C_∞ axis of the spin density on $F^\bullet$ obtained at the fragment level, which corresponds to the orientation of the unpaired $2p$ electron, lies in the symmetry (C_s) plane; when $F\cdots O$ is along the x axis ("x-aligned"), however, the spin density has its C_∞ axis perpendicular to the above-mentioned plane.

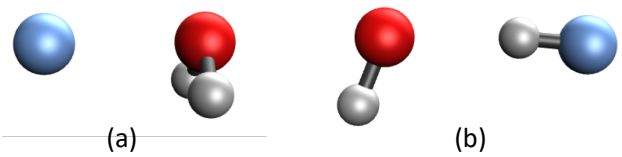

Figure 1: Complexes from the TA13 dataset:[64] (a) $H_2O\cdots F^\bullet$ and (b) $FH\cdots {}^\bullet OH$. As isolated radicals, both $F^\bullet$ and ${}^\bullet OH$ have the odd electron in a degenerate orbital whose orientation is undefined (or "unresolved", as shown in Fig. 2) when imported as frozen orbitals into the radical-molecule complexes (a) and (b).

These two electronic configurations that correspond to the $^2A'$ and $^2A''$ supersystem states, respectively, are no longer degenerate at the supersystem level, resulting in distinct energies for the initial frozen state with a difference of up to 11 kcal/mol. On the other hand, the spherically symmetric $F^\bullet$ radical is indistinguishable at the fragment level during the calculations for the z- and x-aligned complexes, and in fact the same electronic configuration with the β-hole (empty orbital with β spin) residing in $2p_z$ is obtained. One can infer that the arbitrariness in fragment spin orientation will affect any EDA scheme that utilizes the direct or antisymmetrized product of isolated fragment wavefunctions as the initial state, rendering their results non-unique. It is thus highly desirable to develop a protocol that is able to eliminate such arbitrariness in an automated fashion and always yield the same electronic configuration for the initial state regardless of the spatial orientation of the given complex structure.

The remainder of this paper is organized as follows. In Sec. 2, we first briefly summarize the previously developed second-generation ALMO-EDA and adiabatic EDA schemes and then introduce the procedure to resolve the issue arising from the arbitrariness of fragment spin orientation, whose effectiveness is validated with complexes from the TA13 dataset. We then employ these methods to study the intermolecular interactions in several sets of radical-molecule complexes, including complexes involving aromatic radical cations (Sec. 4) and hydroxyl radical (${}^\bullet OH$) complexes with water and aldehydes (Sec. 5). Concluding remarks are given in Sec. 6.

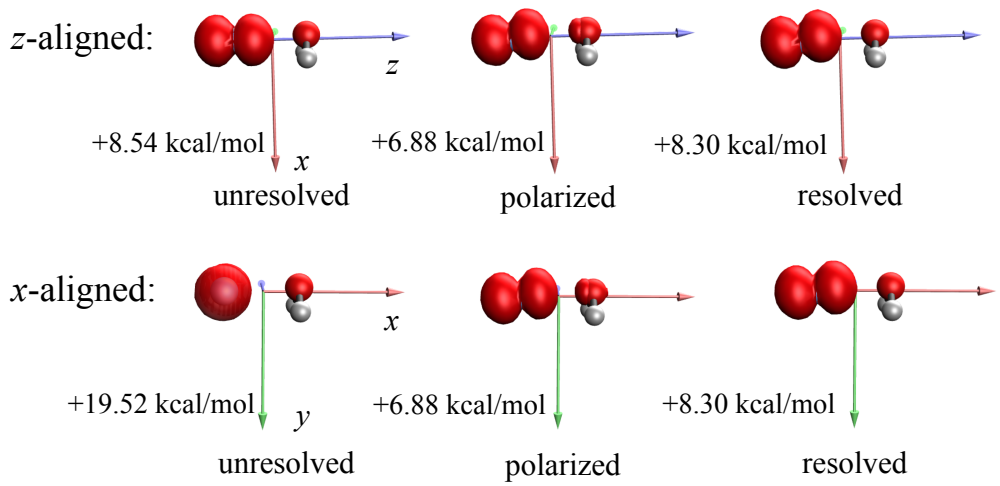

Figure 2: Contour plots (with an isovalue of 0.005 a.u.) of the spin density ($\mathbf{P}_\alpha - \mathbf{P}_\beta$) for the $H_2O\cdots F^\bullet$ complex at different stages of the fragment spin alignment procedure. The $F\cdots O$ connection is along the z axis on the upper panels and x axis the lower ones. The leftmost stage ("unresolved") corresponds to the results obtained directly from fragment SCF calculations, which depend on the orientation of the F orbitals in the lab frame. Orienting the radical electron of $F^\bullet$ along the $F\cdots O$ axis yields an energy increase of 8.5 kcal/mol versus fragments, while a much larger increase of 19.5 kcal/mol occurs when the odd electron is perpendicular. The middle ("polarized") and rightmost ("resolved") stages correspond to the spin densities associated with the converged SCF-MI solution and the resulting depolarized fragment orbitals, respectively. The total energy of each intermediate state is evaluated relative to the sum of isolated fragment (H_2O and $F^\bullet$) energies at the M06-2X/def2-TZVPD level of theory.

2 Method

2.1 Summary of ALMO-EDA Based on Kohn-Sham or Hartree-Fock Electronic Structure Methods

Here we consider an intermolecular interaction energy (ΔE_{INT}) calculated from the supermolecular approach using single-determinant electronic structure methods such as Kohn-Sham (KS)-DFT.[65,66] In the second-generation ALMO-EDA,[42] the total intermolecular in-

teraction energy (ΔE_{INT}) is decomposed as

$$\begin{aligned}\Delta E_{\mathrm{INT}} &= \Delta E_{\mathrm{FRZ}} + \Delta E_{\mathrm{POL}} + \Delta E_{\mathrm{CT}} \\ &= \Delta E_{\mathrm{ELEC}} + \Delta E_{\mathrm{PAULI}} + \Delta E_{\mathrm{DISP}} + \Delta E_{\mathrm{POL}} + \Delta E_{\mathrm{CT}}\end{aligned} \tag{1}$$

The frozen (FRZ) term, ΔE_{FRZ}, captures the energy change upon the formation of the complex without relaxing the fragment wavefunctions, which comprises contributions from permanent electrostatics (ELEC), Pauli repulsion (PAULI), and dispersion (DISP). It is defined as the difference between the energy associated with the antisymmetric product of isolated fragment wavefunctions, which is denoted as E_{FRZ}, and the sum of fragment energies:

$$\Delta E_{\mathrm{FRZ}} = E_{\mathrm{FRZ}} - \sum_{F=1}^{N_{\mathrm{frag}}} E_F \tag{2}$$

The further separation of the FRZ term can be achieved using either the "quasiclassical"[45] or the "orthogonal"[44] decomposition schemes, depending on whether the ELEC component is evaluated using unmodified isolated fragment electron densities. While the "orthogonal" decomposition scheme has the advantage that all the three terms are evaluated in a properly antisymmetrized electronic state, we found that the results given by the "quasiclassical" approach are easier to interpret in many applications. We refer the reader to our previous publications[42,44,45] for details about these two decomposition schemes.

The polarization (POL) term, ΔE_{POL}, is defined as the energy lowering resulting from the relaxation of each fragment in the presence of others *without* any inter-fragment orbital mixings. In ALMO-EDA, the polarized intermediate state (whose energy is denoted as E_{POL}) is obtained by variationally optimizing the supersystem wavefunction subject to the constraint that the molecular orbitals (MOs) of a given fragment are expanded by basis functions belonging to that fragment alone, i.e., the MOs are "absolutely localized" on

fragments and only intra-fragment occupied-virtual orbital mixings are allowed in this procedure. This special variational optimization problem is called "SCF for molecular interaction" (SCF-MI) and can be tackled by solving locally projected SCF equations[67–69] or employing gradient-based optimization methods.[43] The POL term is then evaluated as

$$\Delta E_{\mathrm{POL}} = E_{\mathrm{POL}} - E_{\mathrm{FRZ}} \tag{3}$$

The charge-transfer (CT) term in ALMO-EDA is defined as the energy lowering relative to the polarized state when inter-fragment orbital mixings are permitted, which can be evaluated by taking the difference between the fully relaxed, unconstrained SCF energy (E_{FULL}) and the energy of the polarized state:

$$\Delta E_{\mathrm{CT}} = E_{\mathrm{FULL}} - E_{\mathrm{POL}} \tag{4}$$

One should note that the CT definition in ALMO-EDA does not necessarily imply net flow of charge, as we have demonstrated previously.[50] Instead, it should be understood as an energetic stabilization effect arising from the delocalization of electrons, akin to the well-accepted concept of dative interactions in inorganic chemistry.

As revealed by Eqs. 3 and 4, the polarized yet CT-forbidden state plays a key role in the definition of both the POL and CT terms. In the original ALMO-EDA scheme,[41] the variational subspace of each fragment is spanned by the entire set of atomic orbital (AO) basis functions residing on it, which we refer to as the AO-based ALMO scheme. It has been shown that the separation of POL and CT using this scheme lacks a well-defined basis set limit, since the overlap between basis functions on different fragments increases when larger AO basis sets are employed, rendering the distinction between intra- and inter-fragment relaxations ambiguous.[43,70,71] This drawback of the original method can be addressed by utilizing fragment electric response functions (FERFs) to define the variational subspace of

each fragment,[43] which selects a subset of virtual orbitals on each fragment that are most relevant to its response to an external electric field. The reader can find more details about the FERF approach in our previous work.[43,50]

The scheme summarized above is also referred to as the *vertical* ALMO-EDA since all the energy components are evaluated at a single fixed geometry. While it is a useful tool for understanding the energetics of intermolecular binding, a vertical EDA is unable to directly probe influences of intermolecular interactions on molecular properties. These observable effects, however, are important fingerprints for characterizing intermolecular interactions in experimental studies. To address this gap, we formulated an *adiabatic* ALMO-EDA approach,[46] in which one relaxes the geometry of an intermolecular complex in each of the intermediate states (isolated fragment, FRZ, POL, and fully relaxed) in an ALMO-EDA procedure. The energy components are then defined as the energy difference between the stationary points obtained on two adjacent potential energy surfaces (PESs):

$$\Delta E_{\mathrm{FRZ}}^{(\mathrm{ad})} = E_{\mathrm{FRZ}}^{(0)} - \sum_{F=1}^{N_{\mathrm{frag}}} E_F^{(0)} \tag{5}$$

$$\Delta E_{\mathrm{POL}}^{(\mathrm{ad})} = E_{\mathrm{POL}}^{(0)} - E_{\mathrm{FRZ}}^{(0)} \tag{6}$$

$$\Delta E_{\mathrm{CT}}^{(\mathrm{ad})} = E_{\mathrm{FULL}}^{(0)} - E_{\mathrm{POL}}^{(0)} \tag{7}$$

where the superscripts "ad" are used to differentiate the adiabatic FRZ, POL, and CT terms from their counterparts in vertical ALMO-EDA and "0" denotes energies calculated at stationary points on each PES. A detailed comparison between the vertical and adiabatic ALMO-EDA regarding the differences in their concepts and numerical results is available in ref. 46. Most recently, we introduced two additional intermediate states on which either the

forward or the backward CT is permitted, which are denoted as CTf and CTb, respectively:[52]

$$\Delta E^{(\mathrm{ad})}_{\mathrm{CTf}} = E^{(0)}_{\mathrm{CTf}} - E^{(0)}_{\mathrm{POL}} \tag{8}$$

$$\Delta E^{(\mathrm{ad})}_{\mathrm{CTb}} = E^{(0)}_{\mathrm{CTb}} - E^{(0)}_{\mathrm{POL}} \tag{9}$$

The adiabatic EDA scheme allows one to probe how each interaction component affects the structural and vibrational features of an intermolecular complex. This is achieved by performing geometry optimization followed by harmonic frequency analysis on each PES, which is vastly facilitated by the availability of nuclear gradients (forces) at all levels of an ALMO-EDA calculation: the nuclear forces for standard KS-DFT are employed for the isolated fragment and fully relaxed states, and the forces for the FRZ, POL, CTf, and CTb states have been reported in our previous work.[45,52]

The equations for the vertical and adiabatic ALMO-EDA schemes were derived in spin-orbital notation in our previous publications[43,44,46] such that they can be applied to cases with either restricted or unrestricted orbitals. In the present work, we focus on interactions between radicals and closed-shell species and thus we employ ALMO-EDA with *unrestricted* orbitals, which is denoted as uALMO-EDA in the following discussion.

2.2 Unique Definition of the Frozen State: the "Polarize-then-Depolarize" Approach

We now elaborate the procedure that resolves the arbitrariness in the definition of the frozen state when the open-shell species is highly symmetric and/or has degenerate electronic configurations. Due to degeneracy at the fragment level, it is unlikely that the β-hole will be properly oriented without at least some information about the full system. Therefore, we take advantage of the external perturbation exerted by other fragments, which typically breaks the original degeneracy of MOs belonging to the isolated open-shell species. Such a

perturbation can be fully incorporated through an SCF-MI calculation as in the polarization step of the ALMO-EDA procedure, which is illustrated as the transition from stage (i) to (ii) in Fig. 3.

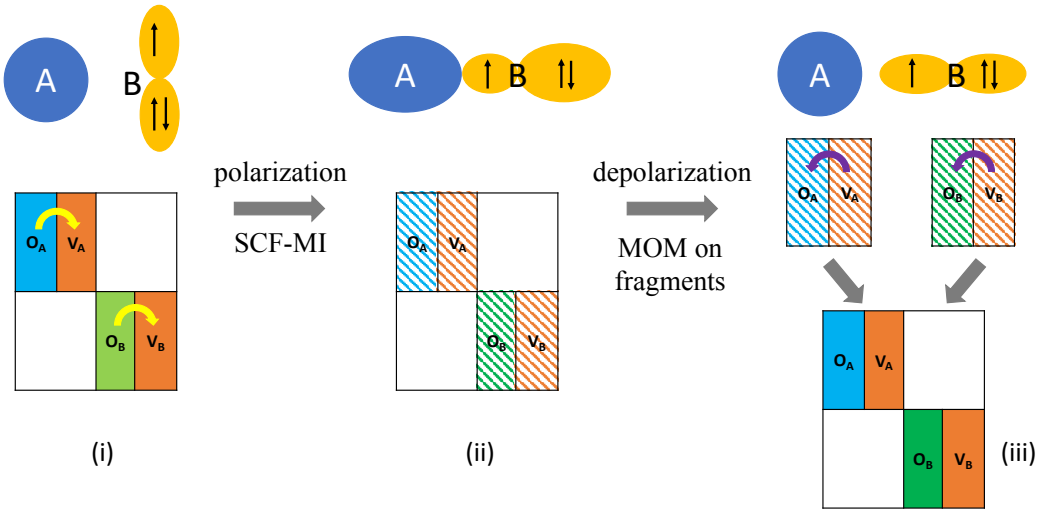

Figure 3: Procedure of the "polarize-then-depolarize" (PtD) approach for uniquely defining the frozen state. Stage (i): the initial frozen state constructed from unaligned fragment orbitals; stage (ii): the polarized wavefunction obtained from an SCF-MI calculation; stage (iii): the final frozen state constructed from aligned fragment orbitals. The upper panels illustrate the electronic configurations of the complex, where fragment A corresponds to a closed-shell moiety and B an open-shell species with degenerate electronic configurations. The lower panels demonstrate the MO coefficients at each stage, where the solid and shaded blocks represent MOs optimized at the isolated fragment level and the polarized ones in the global system, respectively. Note that the MOs on fragment B in the initial (i) and final (iii) frozen states differ from each other, as indicated by slightly different colors.

As the polarized wavefunction is variationally optimized, it provides a possible way to define a single most appropriate electronic configuration for the frozen state. Using polarized fragment orbitals that are represented by the diagonal blocks of the converged ALMO coefficient matrix, one can recalculate the MOs of each fragment without the presence of other fragments, which corresponds to the "depolarization" step in Fig. 3, that is, the transition from stage (ii) to (iii). To prevent the fragment MOs from rotating away from the optimal electronic configuration determined by the polarized ALMOs, we suggest one to

perform these "depolarizing" SCF calculations using the initial maximum overlap method (IMOM)[72,73] combined with the direct inversion of iterative subspace (DIIS)[74] algorithm. After each diagonalization of the Fock matrix, IMOM chooses to occupy the new MOs that have the largest projection into the space spanned by the initial guess orbitals, which thus ensures the resemblance between the polarized and depolarized fragment MOs. In the rest of this paper, we refer to the procedure described above and illustrated in Fig. 3 as the "Polarize-then-Depolarize" (PtD) approach.

We note that the ambiguity in the definition of the frozen state due to the presence of highly symmetric open-shell species was previously discussed in the context of ALMO-EDA for bonded interactions by some of us.[53,54] In the original scheme, which is based on a complete active space(2,2) [CAS(2,2)] description of a single chemical bond,[53] a similar PtD approach was employed: using polarized fragment orbitals (in the spin-flipped state) as the initial guess, the RO wavefunction on each isolated fragment is relaxed, successively, with respect to doubly occupied-virtual (D-V) orbital rotations, singly occupied-virtual (S-V) rotations, and finally all possible orbital rotations. The desired electronic wavefunction given by the polarized fragment orbitals is retained in the resulting fragment orbitals in most cases, thanks to the stepwise manner of handling these orbital rotations. The recent extension of ALMO-MP2-EDA to RO orbitals also adopted the PtD approach,[40] where the resemblance between the polarized and depolarized fragment orbitals was ensured via MOM as in the present paper.

One can use the following criteria to verify whether the fragment spin alignment scheme is functioning properly for a given system: (i) the isolated fragment energies should be identical before and after being aligned; (ii) the energy of the frozen state constructed from MOs of aligned fragments should be no greater than that of the pre-alignment frozen state. In this way, the electronic configuration of the FRZ state is uniquely determined to be the one with the lowest possible energy, by which the arbitrariness in the separation of ΔE_{FRZ} and ΔE_{POL}

in a uALMO-EDA calculation will be eliminated. This scheme should be applied not only in vertical EDA calculations but also in the protocol of adiabatic EDA when one performs geometry optimization and harmonic frequency analysis on the frozen PES, which ensures that the nuclear forces are calculated within the lowest-energy frozen state.

2.3 Implications for the Polarized State: Rehybridization versus inductive relaxation.

The treatment of polarization (POL) differs in a basic way between complexes of closed shell molecules and complexes involving open shell molecules. In the fully closed shell EDA case,[42] POL arises from occupied orbitals on a given fragment mixing with the polarization-specific virtuals (the FERFs)[43] to polarize in the complex environment, and to partly relax Pauli repulsions present in the frozen state. In the case where a radical is involved, the character of the radical orbital may change to more effectively interact with its closed shell partner. Part of those changes can arise from mixing the doubly occupied orbitals with the singly occupied orbital to rehybridize the radical orbital. This rehybridization (REHYB) can be usefully distinguished from the mixing with FERFs, since it has no analog in closed shell complexes. For example, on a single center a radical p orbital may acquire some sp^2 or sp^3 character by mixing with occupied levels.[75] In a large radical cation, the β hole may similarly localize to more favorably interact with a Lewis base (e.g. see Sec. 4.2).

We have developed a new approach to quantify REHYB based on a special SCF-MI calculation that only permits orbital rotations on the open-shell moiety that resemble the doubly-singly (D-S) rotations in the case of an restricted open shell (RO) fragment. Indeed, REHYB describes an effect that is somewhat similar to the concept of rehybridization in the context of bonded ALMO-EDA.[75] Accordingly the rest of POL is assigned to electrical polarization (EL_POL). The details about how the REHYB term is evaluated in uALMO-

EDA are given in Appendix A of the present paper. This enables us to write

$$\Delta E_{\mathrm{POL}} = \Delta E_{\mathrm{REHYB}} + \Delta E_{\mathrm{EL\_POL}} \tag{10}$$

Furthermore, in the context of the adiabatic EDA, it is in principle possible to evaluate the change in geometry from FRZ to REHYB, to determine the contribution of the latter to changes from the FRZ geometry to the POL geometry (or to other properties such as frequency shifts).

We must note that including the REHYB term as part of polarization (as chosen here) is not the only possibility. It can also be first introduced as a fragment preparation energy penalty, *before* the frozen energy is evaluated, such that FRZ includes the energy lowering due to REHYB. This was the choice made in the bonded ALMO-EDA scheme based on spin-projected KS-DFT.[54] In the bonded EDA, the mixing between doubly occupied and singly occupied orbitals (D-S rotation) on each open-shell fragment takes place before the construction of the frozen state, at the cost that the MOs constituting the frozen wavefunction are no longer optimal for each isolated fragment. Rather, the α density is fixed as in the frozen wavefunction, and the β-hole is permitted to relax within the span of the α density, giving rise to an orbital rehybridization term in the bonded EDA.

However, since there is no well-defined separation between doubly and singly occupied orbitals in unrestricted SCF, we found that a procedure resembling the method in ref. 54 could still produce non-unique energies for the frozen state when the system is oriented differently in the lab frame. For this reason, the PtD approach seems to be the only feasible fragment spin alignment scheme for uALMO-EDA. Another advantage of the PtD approach is that the supersystem frozen wavefunction is constructed from stationary MOs of monomers, which vastly simplifies the evaluation of its nuclear forces in adiabatic EDA.

3 Computational Details and Proof-of-Concept Examples

All calculations were performed with a locally modified version of the Q-Chem 5.2 software package.[76] The second-generation ALMO-EDA using unrestricted orbitals was employed to produce all the vertical EDA results, where the FRZ term was further decomposed into ELEC, PAULI, and DISP contributions using the "quasiclassical" scheme as introduced in ref. 45 and truncated fragment virtual orbitals[43] determined by non-orthogonal dipolar and quadrupolar FERFs (the nDQ model) were employed to determine the magnitude of POL and CT. The adiabatic ALMO-EDA results were obtained by optimizing the geometries of isolated fragments and complexes in their FRZ, POL, and fully relaxed states. The geometries were relaxed until the maximum component of the nuclear gradient was smaller than 10^{-4} a.u. and the energy change from the previous step was smaller than 10^{-7} a.u. The vibrational frequencies were computed via a finite-difference approach using the analytical nuclear gradients, for which the step size of each atomic position displacement was set to 10^{-3} Å. Note that the POL state in the adiabatic ALMO-EDA was obtained using the original AO-based ALMO definition[69] since analytic nuclear gradients for the FERF-based approach are currently unavailable.

Unless otherwise specified, the ωB97M-V functional[77] and the def2-TZVPD basis set[78,79] were employed in the vertical and adiabatic EDA calculations reported below. ωB97M-V, a range-separated hybrid (RSH) meta-generalized gradient approximation (mGGA) with the VV10 non-local correlation dispersion correction,[80] was shown to be one of the most accurate density functionals available for non-covalent interactions via extensive benchmarks.[81,82] It also shows decent performance for radical-molecule interactions (the root-mean-square error on the TA13 dataset is 2.75 kcal/mol[81]), which constitute a particularly difficult category of interactions for DFT methods. Besides ωB97M-V, we also generated results with M06-

2X[83] for some of the systems, since this global hybrid mGGA with high percentage of exact exchange (54%) yields the best accuracy on TA13 among the functionals tested in ref. 81. The numerical integration of the exchange-correlation functional was performed on an ultrafine (99, 590) grid (99 radial shells with 590 Lebedev points on each shell), while the SG-1 grid[84] was employed for the integration of VV10.

The fragment spin alignment procedure described in Sec. 2.2 was employed for vertical and adiabatic ALMO-EDA calculations on all radical-molecule complexes investigated in this work. The polarization calculation in this procedure, which is illustrated as the first step in Fig. 3, was performed using AO-based SCF-MI.[69] The fragment coupled-perturbed SCF (CPSCF) equations for FERFs were solved on top of fragments whose spin densities had been properly aligned, as was the evaluation of z-vectors[85] that are required for obtaining the analytic nuclear forces on the frozen surface. We noticed that in several cases, the polarization calculation starting from the initial fragment orbitals will land onto an unstable solution, which then fails to yield the favorably aligned fragment electronic configurations after the depolarization step. To ensure the stability of the SCF-MI solution, we employ the geometric direct minimization (GDM) method[86] to variationally minimize the SCF-MI energy combined with checks of wavefunction stability with respect to on-fragment occupied-virtual mixings. The orbital gradient and Hessian of SCF-MI required in the GDM optimization and wavefunction stability analysis have been previously derived and implemented by some of us.[43] For an SCF-MI solution that is detected to be unstable, a small displacement (orbital rotation) is given along the direction of the eigenvector that corresponds to the most negative eigenvalue of the orbital Hessian before relaunching the GDM optimization.

We demonstrate the effectiveness of the fragment spin alignment procedure using the two complexes from the TA13 dataset shown in Fig. 1. The calculations are performed at the M06-2X/def2-TZVPD level of theory. As we have mentioned above, the energy of the initial frozen state of this complex depends on how the radical orbitals are oriented in

the lab frame. This is an artifact caused by the fact that the frozen state is constructed from isolated fragment MOs. As shown in Fig. 2, the frozen state of the x-aligned complex has an energy that is about 11 kcal/mol higher than that of the z-aligned complex, and the orientation of the empty $2p$ orbital on $F^{\bullet}$ differs in these two frozen complexes. The external field exerted by the interacting water molecule breaks the degeneracy of the $2p$ orbitals, and the polarization step indeed leads to the same electronic state ($^2A'$) for both the z- and x-aligned complexes (see the two middle panels in Fig. 2). We note that for the x-aligned complex, the SCF-MI wavefunction stability analysis and correction procedure described above is required, as otherwise one would obtain an unstable SCF-MI solution that resembles its "unresolved" state. The final frozen states obtained from depolarizing the stable SCF-MI solution for these two complexes also show no difference, indicating that the arbitrariness in defining the frozen state has been removed. The final, uniquely defined frozen state has an energy that is lower than the initial frozen state of either the z-aligned or x-aligned complex, and their spin density profiles, as shown in the rightmost panels of Fig. 2), closely resemble that of the polarized state. The C_∞ axis of the empty $2p$ orbital lies in the C_s plane while forming a small angle with the F$\cdots$O direction, which differs from that in the initial ("unresolved") frozen states of both the z- and x-aligned complexes, where the C_∞ axis is always along the z direction (in and perpendicular to the symmetry plane, respectively). This further emphasizes the necessity of employing the fragment spin alignment procedure for one to obtain a uniquely defined, lowest-energy frozen state.

The inconsistency in the resulting FRZ and POL energies when the complex is oriented differently in lab coordinates also occurs for two other water-halogen complexes, $H_2O\cdots Cl^{\bullet}$ and $H_2O\cdots Br^{\bullet}$, in the TA13 dataset. As shown in Table 1, without the PtD fragment spin alignment procedure the discrepancy in the FRZ term reaches $\sim$10 kcal/mol for all three systems depending on whether the complex is z- or x-aligned, and the magnitude of POL varies correspondingly. When the PtD procedure is applied, on the other hand, the resulting

Table 1: Dependence of the FRZ and POL energies (in kcal/mol) of uALMO-EDA on the orientation of the $H_2O\cdots X^\bullet$ (X = F, Cl, Br) complexes from the TA13 dataset under the lab coordinate. The "axis" column indicates the direction of $O\cdots X$ as in Fig. 2. Note that POL energy here is calculated using the AO-based ALMO definition such that it corresponds to energy difference between the "polarized" state and the "unresolved" (no PtD) or "resolved" (with PtD) frozen state.

	axis	no PtD		with PtD	
		FRZ	POL	FRZ	POL
$H_2O\cdots F^\bullet$	z	8.54	-1.66	8.30	-1.42
	x	19.52	-12.64	8.30	-1.42
$H_2O\cdots Cl^\bullet$	z	1.29	-1.68	1.18	-1.57
	x	10.80	-11.19	1.18	-1.57
$H_2O\cdots Br^\bullet$	z	0.98	-1.98	0.86	-1.86
	x	11.19	-12.19	0.86	-1.86

FRZ and POL energies turn out to be independent of the orientation of each complex.

We now move to the $FH\cdots{}^\bullet OH$ complex, whose spin densities at different stages of the alignment procedure are shown in Fig. 4. Differing from the $H_2O\cdots F^\bullet$ example, the same electronic configuration for the frozen state is obtained regardless of the set-up of the lab coordinates, where the C_∞ axis of oxygen's empty $2p$ orbital lies in the molecular plane and orthogonal to the O−H σ-bond (see the leftmost panel in Fig. 4). Nonetheless, such an electronic configuration of the frozen state ($^2A'$) is *not* the energetically most favorable one, which is the one shown in the rightmost panel with the $2p$ orbital perpendicular to the molecular plane ($^2A''$), with an energy that is 3.6 kcal/mol lower. According to our discussion above, this energetically more favorable configuration should be adopted as the correct frozen state. We demonstrated that one can achieve this by using the PtD procedure, as the polarization step manages to identify that within the stable SCF-MI solution the empty $2p$ orbital on the O atom should be perpendicular to the molecular plane, which is shown in the mid-panel of Fig. 4. The final frozen state obtained from the depolarization step then inherits the feature of the stable SCF-MI solution.

With the two examples above, we have shown how the PtD fragment spin alignment pro-

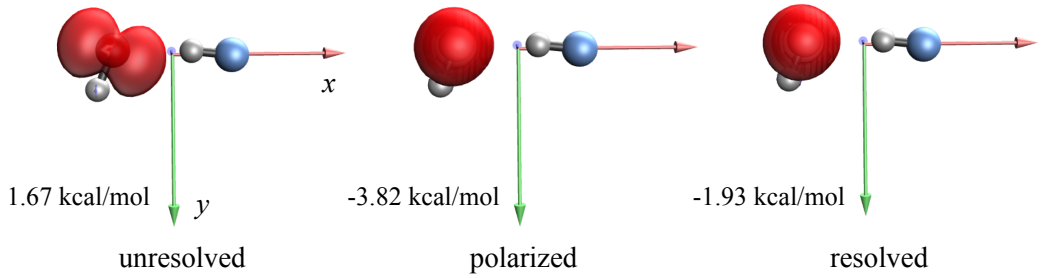

Figure 4: Contour plots of the spin density of the FH···•OH complex. All atoms in the complex lie in the xy-plane. The other plotting and computational details are the same as in Fig. 2.

cedure described in Fig. 3 eliminates the arbitrariness in defining the frozen state in uALMO-EDA calculations. In the following two sections, we employ uALMO-EDA augmented with these additional steps to investigate several examples of radical-molecule interactions.

4 Application to Complexes of Aromatic Radical Cations

4.1 Benzene Dimer Radical Cation

The benzene dimer radical cation is a prototypical open-shell π-dimer system and it was previously investigated by Gonthier and Sherrill using density-fitted SAPT0(UHF).[30] Here we employ uALMO-EDA to study the face-to-face stacked (sandwiched) and T-shaped configurations of the benzene dimer radical cation, whose structures are illustrated in the insets of Figs 5 and 6, respectively. The geometries of these complexes are taken from ref. 30 so that our EDA results can be directly compared to the results of SAPT0(UHF).

We first validate the use of the ωB97M-V functional for these radical-neutral interactions. As shown in Figs. 5(a) and 6(a), the resulting total interaction energies (denoted as "Total") are in good agreement with the reference values from ref. 30 calculated with the frozen natural orbital (FNO) variant[87,88] of the EOM-IP-CCSD (equation-of-motion coupled-cluster singles and doubles for ionization potential) ansatz[89] despite the marginal overestimation at short

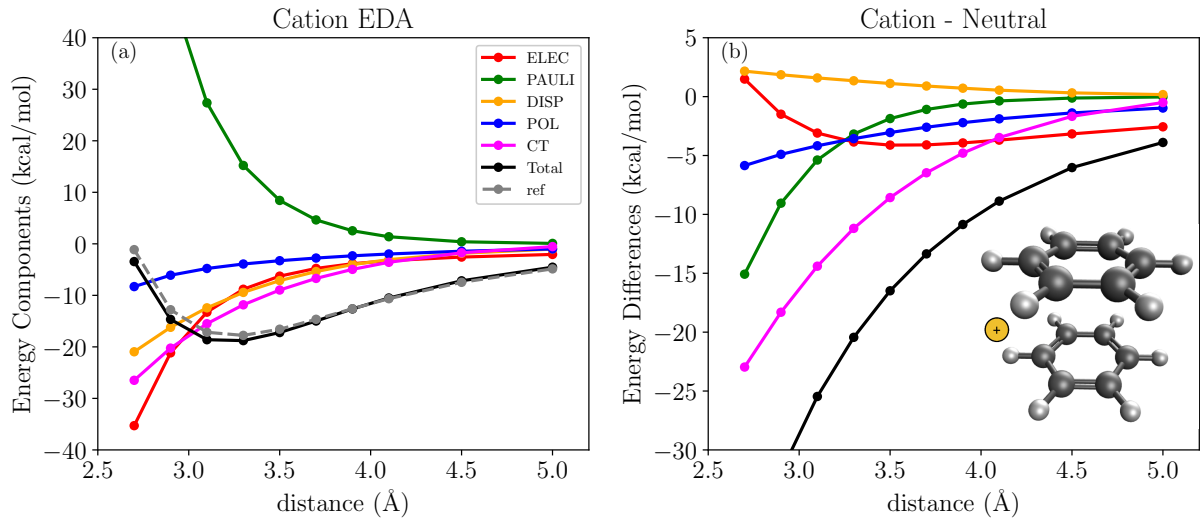

Figure 5: ALMO-EDA results (in kcal/mol) for the sandwiched benzene dimer radical cation at varying interplanar distances (left panel) and the comparison against EDA results for the charge-neutral counterpart (right panel). The energy difference in each term is evaluated as $\Delta E_X^{\mathrm{C}} - \Delta E_X^{\mathrm{N}}$, where "$X$" denotes a given energy component, and "C"/"N" represents the results for the cationic/neutral species. The ALMO-EDA results are calculated at the ωB97M-V/def2-QZVPPD level of theory, and the reference values are from ref. 30.

range for the sandwiched configuration. In Fig. S1 in the Supporting Information (SI) we further compare the performance of ωB97M-V against that of M06-2X and SAPT0(UHF). For the sandwiched dimer, M06-2X overestimates the interaction energy more significantly than ωB97M-V at equilibrium and longer distances, while the SAPT0(UHF) results are markedly underbound except for the longest distances. For the T-shaped dimer, M06-2X yields overbound results across the entire plotting range, while SAPT0(UHF) under- and overestimates the interaction energy in the short and long ranges, respectively, resulting in a skewed potential energy curve (PEC). ωB97M-V offers superior accuracy than either M06-2X or SAPT0(UHF) for the interaction PECs of these two benzene dimer radical cation configurations.

The sandwiched benzene dimer radical cation is more strongly bound than the T-shaped isomer by $\sim$7 kcal/mol comparing their equilibrium interaction energies shown in Figs. 5(a)

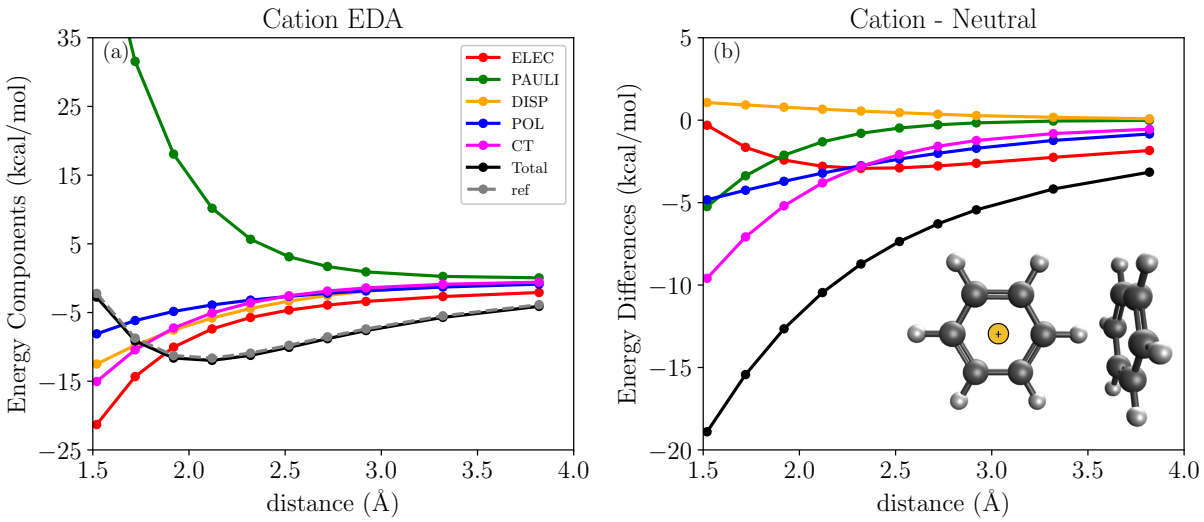

Figure 6: ALMO-EDA results (in kcal/mol) for the T-shaped benzene dimer radical cation at varying C−H$\cdots\pi$ distances (left panel) and the comparison against EDA results for the charge-neutral counterpart (right panel). The computational and plotting details are the same as in Fig. 5.

and 6(a)). This differs from the case of the neutral benzene dimer where the T-shaped configuration has a more stable equilibrium structure (see Tables S1 and S2 in the SI). The uALMO-EDA results for the sandwiched dimer (Fig. 5(a)) suggest that ELEC, DISP, and CT all contribute significantly to the binding of this complex, among which CT makes the largest contribution around the equilibrium distance, while POL, on the other hand, only plays a secondary role compared to other attractive energy components. For the T-shaped dimer (Fig. 6(a)), ELEC makes the largest contribution among all energy components at equilibrium, which is followed by DISP and CT, and POL is also of greater relative importance compared to its role in the sandwiched dimer. We note that starting from an initial guess with charge and spin localized on one of the monomers, the full SCF calculation for the T-shaped dimer would land onto an unstable solution, whose spin density profile is demonstrated in Fig. S2(a) in the SI; our EDA results, on the other hand, are based upon the stable SCF solution whose spin density profile is shown in Fig. S2(b).

While uALMO-EDA and SAPT0(UHF) are two approaches formulated rather differently,

they yield similar trends for the composition of interaction energies in the sandwiched and T-shaped dimers (see Fig. 2 and Fig. 3(a) in ref. 30 for the SAPT0(UHF) results). To be more specific, we find that PECs for the electrostatics ("Elst"), exchange ("Exch"), and induction ("Ind") terms in SAPT0(UHF) closely resemble those for the ELEC, PAULI, and DISP terms in uALMO-EDA, respectively. The δHF term in SAPT0(UHF), which accounts for the high-order induction effect that is not captured by the perturbation theory, roughly corresponds to the CT term in uALMO-EDA although the magnitude of the former is notably smaller. The underestimation of the CT energy is likely to be the main reason why SAPT0(UHF) markedly underbinds the sandwiched benzene dimer radical cation. The dispersion ("Disp") contribution predicted by SAPT0(UHF), on the other hand, turns out to be slightly more attractive than its counterpart in uALMO-EDA.

The comparison between the EDA results for the cationic and neutral sandwiched dimer (Fig. 5(b)) reveals that the substantially stronger binding in the radical cation system mainly results from its enhanced CT because of the existence of a β-hole on one of the benzene monomers. At $r = 3.3$ Å, CT stabilizes the radical cation system by over 11 kcal/mol. The β-hole also renders the PAULI term less repulsive and DISP term less attractive, as one would expect. The positive charge on one of the monomers also enhances the polarization effect and renders the long-range electrostatics more attractive, for which the differences from the neutral dimer results are within 5 kcal/mol except at the shortest distance. These trends also hold for the T-shaped dimer (Fig. 6(b)), albeit with a less remarkable difference in the CT component. We note that unlike other terms, the difference between the magnitude of the ELEC term in cationic and neutral complexes does not vary monotonically with the intermolecular distance, which holds for both the sandwiched and T-shaped isomers. For the sandwiched dimer, the trend is even reversed at the shortest distance (2.7 Å), i.e., the ELEC term becomes more favorable in the neutral complex. This can be explained by the governing role of charge penetration effect in the short-range electrostatics,[45,90] which depends on the

overlap of monomer electron densities and thus is less pronounced in the electron-deficient cationic dimers.

4.2 Nucleophilic Addition to Benzene$^{+\bullet}$ and Naphthalene$^{+\bullet}$ by Pyridine

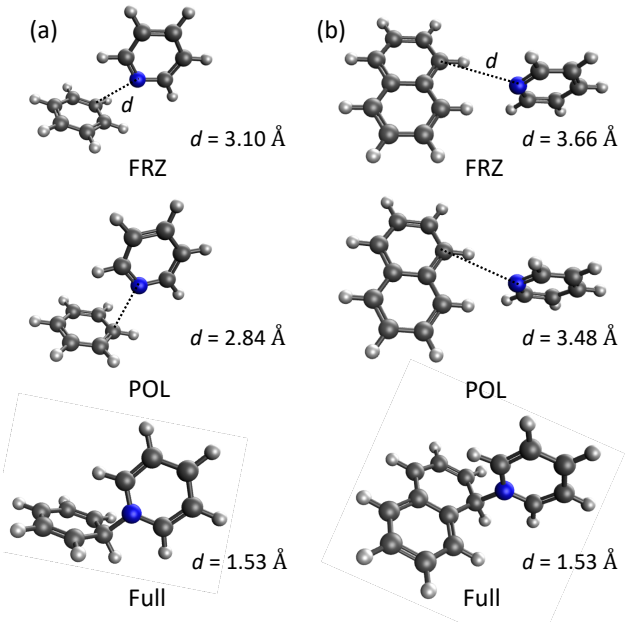

Figure 7: Structures of the (a) Bz$^{+\bullet}$−Py and (b) Naph$^{+\bullet}$−Py complexes obtained at the FRZ, POL, and full SCF levels of adiabatic ALMO-EDA. d refers to the distance between the N atom of pyridine and the closest C atom on the aromatic radical cation moiety.

We revisit the benzene$^{+\bullet}$ − pyridine (Bz$^{+\bullet}$−Py) and naphthalene$^{+\bullet}$ − pyridine (Naph$^{+\bullet}$–Py) complexes that were previously investigated by Peverati et al.[13] The geometries of these complexes optimized with ωB97M-V/def2-TZVPD are shown in the bottom two panels of Fig. 7, in which the shortest C−N distance is 1.53 Å for both complexes. This result is in excellent agreement with the previously reported values (1.53 Å for both complexes)[13] based on geometry optimization at the ωB97X-V[91]/cc-pVTZ[92] level of theory. We then performed vertical uALMO-EDA calculations with the same model chemistry at the equilibrium structures of these complexes, and the results are summarized in Table 2. It was

found by Peverati et al. that despite the almost identical C−N bond lengths in $Bz^{+\bullet}$−Py and $Naph^{+\bullet}$−Py, their binding energies differ strikingly by ∼16 kcal/mol (calculated using ωB97X-V/pc-3[93,94]), and the stronger binding of $Bz^{+\bullet}$−Py was attributed to its less pronounced Pauli repulsion according to the EDA results in ref. 13. Our results in Table 2 agree with the previous findings, where the $Bz^{+\bullet}$−Py complex is more strongly bound by 15.7 kcal/mol and its PAULI term is ∼20 kcal/mol less repulsive than that of $Naph^{+\bullet}$−Py. We note that the binding energy (BIND) in Table 2, as in ref. 13, describes the energy change upon the formation of a complex relative to the individually relaxed monomers, and thus it includes both the total interaction energy (INT) and monomer geometry distortion (GD) energies, i.e., the energy penalty for each fragment to change its geometry into the one that it possesses in the complex. According to the results in Table 2, the GD term also makes a contribution of 4.5 kcal/mol to the more favorable binding energy in $Bz^{+\bullet}$−Py, which is close to the previously reported value (5.3 kcal/mol) as well.[13] These results indicate that the two combinatorially designed functionals ωB97X-V and ωB97M-V, when paired with sizable basis sets (triple- or quadruple-ζ), produce rather consistent results for these two radical-neutral complexes not only in terms of the total binding strength but even for each energy component. The consistency in EDA results also suggests that the issue related to the non-unique definition of the frozen state does not emerge for this set of systems, since the calculations in ref. 13 were performed without the fragment spin alignment procedure.

While the magnitude of ELEC, DISP, and CT shows minimal difference between these two complexes, the POL contribution is notably more favorable for $Naph^{+\bullet}$−Py. This was also noticed in the previous work and was then rationalized by the potentially larger energy lowering upon localizing the β-hole in $Naph^{+\bullet}$, as the delocalization of the positive charge could be more extensive in $Naph^{+\bullet}$ than in $Bz^{+\bullet}$. We quantified this effect by performing the partition (see Sec. 2.3, and Appendix A) of polarization into rehybridization (REHYB) and electrical induction (EL_POL) contributions. On this basis, we identified that the con-

Table 2: ALMO-EDA results (in kcal/mol) for the $Bz^{+\bullet}$−Py and $Naph^{+\bullet}$−Py complexes at their equilibrium geometries calculated at the ωB97M-V/def2-TZVPD level of theory. The differences between the EDA results for these two systems are shown in the rightmost column. To make the results comparable with those in ref. 13, the ELEC, PAULI, and DISP terms are obtained using the "orthogonal" frozen energy decomposition scheme.[44]

	$Bz^{+\bullet}$−Py	$Naph^{+\bullet}$−Py	Difference
FRZ[a]	152.7	168.8	16.1
ELEC	-75.2	-77.5	-2.2
PAULI	245.5	265.1	19.6
DISP	-17.6	-18.8	-1.2
REHYB	-8.3	-14.9	-6.6
EL_POL	-116.5	-116.3	0.2
POL[b]	-124.8	-131.2	-6.4
CT	-91.6	-90.3	1.3
TOTAL	-63.7	-52.6	11.1
GD	23.3	27.8	4.5
BIND[c]	-40.4	-24.8	15.6

[a] FRZ = ELEC + PAULI + DISP
[b] POL = REHYB + EL_POL
[c] BIND = GD + INT

siderably more favorable polarization energy in $Naph^{+\bullet}$−Py almost fully arises from its more substantial energy lowering associated with the electron density reorganization that localizes the β-hole, i.e., the REHYB term (see Table 2); the EL_POL energies for these two complexes, on the other hand, are nearly identical to one another. The more significant reorganization of electron density in the $Naph^{+\bullet}$−Py complex is further demonstrated by visualizing the change in spin density upon the rehybridization step (Fig. 8), revealing that a greater amount of spin density is depleted from the aromatic system and gathered around the C atom attacked by pyridine in $Naph^{+\bullet}$−Py (the right panel).

Due to the relatively short intermolecular distances in these two complexes, a vertical EDA inevitably yields strongly repulsive FRZ terms that are dominated by PAULI repulsion. In addition, POL is predicted to contribute more than CT to the formation of these 2-center 3-electron (2c-3e) bonds, which at first glance is a somewhat counterintuitive result.

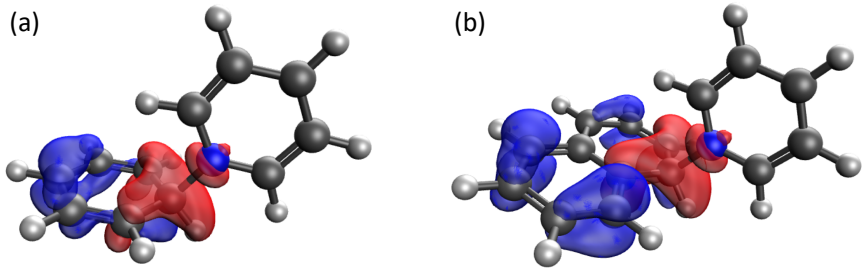

Figure 8: Reorganization of the spin density on (a) $Bz^{+\bullet}$ and (b) $Naph^{+\bullet}$ upon the localization of the β-hole. The contours (isovalue = 0.001 a.u.) show the difference between the spin density ($\mathbf{P}_\alpha - \mathbf{P}_\beta$) of the "rehybridized" state (after the special SCF-MI calculation described in Appendix A) and that of the FRZ state. The red color indicates regions with an increase in α-electron density or decrease in β-electron density while the blue color indicates the opposite.

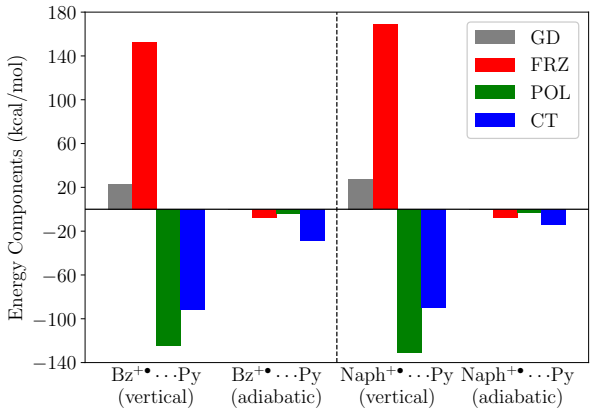

Figure 9: Comparison between the vertical and adiabatic ALMO-EDA results for the $Bz^{+\bullet}$−Py and $Naph^{+\bullet}$−Py complexes. Note that the GD term is zero by definition within adiabatic EDA.

However, similar trends were observed previously for closed-shell Lewis acid-base adducts such as NH_3−BH_3 and BH_3−CO.[46,50] To obtain a complementary view of these interactions, we also investigate $Bz^{+\bullet}$−Py and $Naph^{+\bullet}$−Py using the adiabatic uALMO-EDA, which involves optimizing the complex geometries on the POL and FRZ surfaces. As shown in Fig. 7, the closest C−N distance in $Bz^{+\bullet}$−Py and $Naph^{+\bullet}$−Py is roughly doubled when CT is absent, highlighting the importance of CT as a driving force in the formation of these complexes. The bending of the C−H bond relative to the aromatic plane is a by-product of charge transfer, since the bending angle is roughly zero at the POL and FRZ levels (see

Table S3 in the SI). It is noteworthy that the optimal structures of $Naph^{+\bullet}$−Py on the FRZ and POL surfaces are of C_{2v} symmetry, which drastically differs from its fully relaxed structure and the structure of $Bz^{+\bullet}$−Py optimized on the FRZ and POL surfaces. The energy components obtained from the adiabatic EDA, as shown in Fig. 9, are in sharp contrast with the vertical EDA results. All energy components are of much smaller magnitude than those given by vertical EDA, as in adiabatic EDA the cost to overcome Pauli repulsion is absorbed in each energy component. The results suggest that these complexes are only loosely bound at the FRZ and POL levels, further emphasizing the governing role of CT in the complexation procedure. Under the adiabatic picture, the stronger binding in $Bz^{+\bullet}$−Py is mainly attributed to its greater strength of CT, which is ∼15 kcal/mol more favorable than that in $Naph^{+\bullet}$−Py, while the differences in the other two energy components are minimal (see Table S3 in the SI for details). This conclusion is consistent with the fact that $Bz^{+\bullet}$ has a higher adiabatic electron affinity (9.15 eV) than that of $Naph^{+\bullet}$ (8.01 eV), that is, $Bz^{+\bullet}$ is more susceptible to the electron-donation of Py (the electron affinity values are computed using ωB97M-V/def2-TZVPD).

5 Application to Hydroxyl Radical ($^{\bullet}$OH) Complexes

5.1 $^{\bullet}$OH–Water Complexes

In atmospheric chemistry, the hydroxyl radical ($^{\bullet}$OH) mainly comes from ultraviolet photolysis of ozone in the presence of water vapor.[95] With non-negligible abundance (∼10^6 molecules/cm^3), atmospheric $^{\bullet}$OH serves as the initiator of many radical chain reactions, such as the oxidation of volatile organic compounds.[95–97] $^{\bullet}$OH can form complexes with H_2O because water's much larger concentration in the troposphere (∼10^{17} molecules/cm^3).[98] Moreover, recent studies have shown that water can participate in many gas-phase reactions and influence the reaction kinetics.[5–10,99] For instance, Abel et al. found that water can ac-

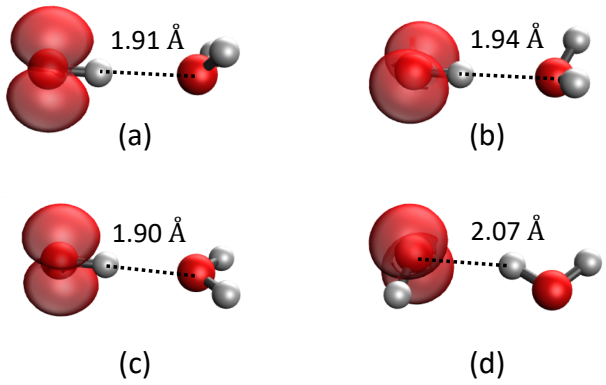

Figure 10: Structures of the $^{\bullet}$OH(H_2O) complex optimized using ωB97M-V/def2-TZVPD with contour plots of the associated electronic spin densities (with an isovalue of 0.005 a.u.): (a) the global minimum with an $^2A'$ electronic state; (b) the structure optimized in the low-lying excited state $^2A''$; (c) the transition structure between two equivalent $^2A'$ global minima that are symmetric with regard to the plane of the H_2O molecule; (d) a local minimum with $^{\bullet}$OH serving as the H-bond acceptor. The O$\cdots$H distance for each H-bond is given.

celerate the reaction between $^{\bullet}$OH and acetaldehyde (CH_3CHO) by lowering the reaction barrier, behaving as a catalyst.[5]

Here we employ the uALMO-EDA to probe the interactions between $^{\bullet}$OH and H_2O molecules, which were recently investigated by Hernandez et al. in a combined experimental and computational study.[98] First we focus on the binary complex $^{\bullet}$OH(H_2O), whose minimum-energy structure, as shown in Fig. 10(a), is of C_s symmetry, which is consistent with the spectroscopic characterization.[100] The β-hole lies in the symmetry plane and thus the corresponding electronic state is of $^2A'$ symmetry. We note that wavefunction stability analysis and correction are required to ensure that the true minimum-energy structure is obtained, since otherwise the geometry optimization would have been performed on the PES of a low-lying excited state ($^2A''$), in which the β-hole is perpendicular to the symmetry plane (Fig. 10(b)). At their respective minima, the energy of the $^2A''$ state is 0.33 kcal/mol ($\sim$115 cm^{-1}) higher than that of the $^2A'$ state, which is in good agreement with the previously reported energy differences between them.[18,100] The vertical ALMO-EDA results for the $^2A'$ and $^2A''$ states (Table S4 in the SI) at the minimum-energy geometry (Fig. 10(a))

Table 3: Adiabatic EDA results for four isomers of $^{\bullet}OH(H_2O)$ ((a)–(d) in Fig. 10) and the "down-up" configuration of $^{\bullet}OH(H_2O)_2$ at the FRZ, POL, and fully relaxed levels. For the binary complexes (a)–(d), ΔE_{bind} represents the energy lowering relative to the total energy of relaxed monomers, while for the ternary complex $^{\bullet}OH(H_2O)_2$ it is calculated relative to the sum of the energy of an equilibrium water dimer and that of a free $^{\bullet}OH$. The tilt angle (°) refers to the angle between the O−H bond in $^{\bullet}OH$ and the bisector of the H_2O molecule, r_{OH} (in Å) and ω_{OH} (in cm^{-1}) denote the length of the radical O−H bond and its stretching frequency, respectively, $\Delta\omega_{\text{OH}}$ denotes the shift relative to ω_{OH} of a free $^{\bullet}OH$, and ω_1 denotes the lowest harmonic frequency obtained. The vibrational frequencies are calculated with all the H atoms on H_2O deuterated in order to decouple the OH stretch modes of $^{\bullet}OH$ and H_2O. At the employed level of theory (ωB97M-V/def2-TZVPD), r_{OH} and ω_{OH} for the free $^{\bullet}OH$ are 0.974 Å and 3734 cm^{-1}, respectively.

	FRZ	POL	FULL	FRZ	POL	FULL	FRZ	POL	FULL
	(a)			(b)			$^{\bullet}OH(H_2O)_2$		
ΔE_{bind}	-3.68	-4.52	-5.87	-3.50	-4.30	-5.54	-6.18	-7.88	-10.53
tilt angle	147.3	144.8	139.4	141.9	139.8	134.1	–	–	–
r_{OH}	0.974	0.976	0.982	0.975	0.976	0.982	0.976	0.979	0.990
ω_{OH}	3746	3718	3586	3741	3713	3585	3724	3672	3446
$\Delta\omega_{\text{OH}}$	12	-16	-148	7	-21	-149	-10	-62	-288
	(c)			(d)					
ΔE_{bind}	-3.65	-4.47	-5.77	-2.26	-2.68	-3.60			
r_{OH}	0.974	0.976	0.981	0.974	0.974	0.975			
ω_{OH}	3748	3724	3610	3730	3729	3717			
$\Delta\omega_{\text{OH}}$	14	-10	-124	-4	-5	-17			
ω_1	$51i$	$72i$	$96i$	$35i$	45	62			

suggest that the $^2A'$ complex is energetically more stable mainly because of its more favorable ELEC and less repulsive PAULI terms. Fig. 10(c) shows the structure of the transition state (TS) between two equivalent minima of the $^2A'$ complex that are mirror images of one another with respect to the H_2O plane. This TS (with one imaginary frequency of $96i$ cm^{-1}) was obtained by geometry optimization subject to C_{2v} symmetry, such that all atoms reside in the same plane. There is also an $^2A''$ energy minimum featuring a co-planar structure (Fig. 10(d)), in which the $^{\bullet}OH$ radical serves as an H-acceptor rather than a donor. Structure (d) is less strongly bound than the most stable structure, (a), by over 2 kcal/mol.

We applied the adiabatic ALMO-EDA to binary complexes (a)–(d), yielding the results shown in Table 3. Note that due to the existence of two closely lying electronic states,

the PtD procedure is indispensable for getting the correct results for the FRZ state, and wavefunction stability needs to be checked and corrected for the POL and FULL surfaces as well. Similar to the water dimer,[46] the main driving force for the formation of these H-bonds is the FRZ interaction, while POL and CT also make rather significant contributions to binding. The angle between the direction of H$-$O$^\bullet$ and the bisector of the H_2O molecule, denoted as the "tilt angle" in Table 3, is quite far from 180° at all stages for complex (a). Complex (c), on the other hand, is characterized to be a TS across the board as indicated by its consistently imaginary ω_1 (Table 3), even although one may suppose that this C_{2v} structure is more favored by the dipole-dipole electrostatic interaction between $^\bullet$OH and H_2O. Complex (b), which is in a different electronic state than (a) and (c), turns out to be less bound than either of them at all stages. The shifts in its observables show similar trends as those in complex (a) in general, while it is noteworthy that the tilt angle in (b) is consistently $\sim$5° smaller than that in (a).

For complexes (a)–(c), one can observe significant elongation of the radical O$-$H bond and a red shift of over 100 cm^{-1} in its stretch frequency relative to that of free $^\bullet$OH. The adiabatic EDA results suggest the dominant role of CT in giving rise to these effects, which, once again, is in good agreement with our previous investigation of closed-shell systems such as the water dimer and the $OH_2\cdots Cl^-$ complex.[46] Interestingly, the radical OH stretch frequency is slightly blue-shifted on the FRZ surface for these three complexes ((a)–(c)) despite the marginal increase in the bond length, which differs from the normal correlation between the bond length and stretching frequency for the proton-donating group X$-$H in H-bonding complexes.[48,101]

Moving to complex (d), the $^\bullet$O$-$H bond is elongated and red-shifted at all levels of the adiabatic EDA despite the effects being far less pronounced. The relatively large shift from POL to FULL suggests that the CT from $^\bullet$OH to H_2O also weakens the $^\bullet$O$-$H bond. We note that with FRZ interaction only, isomer (d) turns into an unstable transition structure

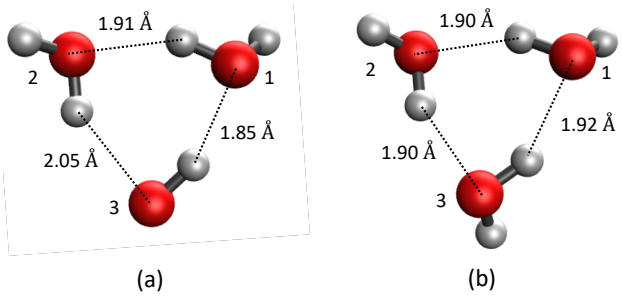

Figure 11: Equilibrium geometries of (a) $^{\bullet}OH(H_2O)_2$ and (b) the H_2O trimer optimized with ωB97M-V/def2-TZVPD. Indexes "1", "2", and "3" are used to refer to each fragment in the many-body expansion.

as indicated by its imaginary ω_1, suggesting that there exists no stable energy minimum on the FRZ surface when $^{\bullet}OH$ serves as the H-acceptor.

We now turn to the ternary complex $^{\bullet}OH(H_2O)_2$, whose optimized geometry is shown as Fig. 11(a). The $^{\bullet}OH$ radical (fragment 3) forms one H-bond with each of the water molecules (fragments 1 and 2), serving as the proton donor and acceptor, respectively. The non-H-bonded H atoms of 1 and 2 are below and above the plane of three O atoms, respectively, and it is thus labeled as the "down-up" complex under the convention of ref. 98. The $^{\bullet}OH\cdots OH_2$ H-bond is 0.06 Å shorter than that in the most stable binary complex (Fig. 10(a)), and the other H-bond, which we denote as $HOH\cdots{}^{\bullet}OH$, is also 0.02 Å shorter than that in the corresponding binary complex (Fig. 10(d)). The unpaired electron in the stable structure is approximately perpendicular to the plane of three oxygen atoms (see Fig. S3 in the SI), so the orientation of the β-hole relative to the 1−3 and 2−3 H-bonds resembles those in binary complexes (a) and (d), respectively.

We first treat the two neutral H_2O molecules as a whole and investigate their effects on $^{\bullet}OH$ using the adiabatic EDA (see Table 3). The equilibrium binding energy, which is evaluated relative to the energies of an equilibrium water dimer and a free $^{\bullet}OH$, is less than twice of that in binary complex (a). The lengthening of the radical O−H bond and the red shift in its vibrational frequency, however, are both almost exactly doubled compared to

Table 4: ALMO-EDA results (in kcal/mol) for the MBE of the $^{\bullet}OH(H_2O)_2$ complex and the H_2O trimer. The meaning of indices "1", "2", and "3" are shown in Fig. 11. The 3-body term (ΔE_{3b} is defined as the difference between the total interaction energy (ΔE_{123}) and the sum of three 2-body terms (ΔE_{12}, ΔE_{13}, and ΔE_{23}).

	$OH^{\bullet}(H_2O)_2$				
	ΔE_{12}	ΔE_{13}	ΔE_{23}	ΔE_{3b}	ΔE_{123}
FRZ	-1.61	-0.92	-1.39	-0.03	-3.96
POL	-1.30	-1.79	-0.78	-1.78	-5.65
CT	-1.90	-2.58	-1.31	-0.61	-6.40
Total	-4.81	-5.28	-3.49	-2.42	-16.00
	H_2O trimer				
	ΔE_{12}	ΔE_{13}	ΔE_{23}	ΔE_{3b}	ΔE_{123}
FRZ	-1.49	-1.37	-1.50	-0.08	-4.43
POL	-1.35	-1.25	-1.35	-1.82	-5.77
CT	-2.01	-1.79	-1.99	-0.62	-6.41
Total	-4.86	-4.40	-4.83	-2.52	-16.61

those in the most stable binary complex. Energy decomposition results suggest that FRZ still makes the largest contribution to the binding between $^{\bullet}OH$ and $(H_2O)_2$ within the adiabatic picture, although the significance of both POL and CT is slightly increased. Differing from the binary complexes (a)–(c), the radical O−H bond is already elongated and red-shifted at the FRZ level, and the red-shifting effect of POL is nearly doubled for the ternary complex. CT, on the other hand, still remains the main contributor to the changes in r_{OH} and ω_{OH}. We note that the frequency shifts obtained for the binary (a) and ternary ("down-up") complexes are in good agreement with the unscaled unrestricted MP2 frequencies reported by Hernandez et al.,[98] which are -131 and -262 cm^{-1}, respectively.

To better understand the interactions in the ternary $^{\bullet}OH(H_2O)_2$ complex, we apply vertical ALMO-EDA to the full many-body expansion (MBE) of its interaction energy:

$$\Delta E = \Delta E_{12} + \Delta E_{13} + \Delta E_{23} + \Delta E_{123}. \tag{11}$$

Here the 2-body interactions are defined as $\Delta E_{12} = E_{12} - E_1 - E_2$, and the single 3-body correction is $\Delta E_{123} = E_{123} - \Delta E_{12} - \Delta E_{13} - \Delta E_{23} - E_1 - E_2 - E_3$. Results for the radical complex can be compared to those for the MBE of an equilibrium water trimer (Fig. 11(b)), as summarized in Table 4. For simplicity, the ELEC, PAULI, and DISP terms (whose MBE is given in Table S5) are combined altogether as the FRZ term in Table 4.

In terms of the total interaction energy, the H_2O trimer is more strongly bound than $^{\bullet}OH(H_2O)_2$ by ∼0.6 kcal/mol, and the EDA results suggested that this difference mainly stems from the FRZ term rather than POL and CT. Turning to the MBE results, the 3-body effect (ΔE_{3b}) is cooperative in both complexes for all three energy components (FRZ, POL, and CT), with the H_2O trimer showing slightly higher cooperativity in all of them. The overall difference between the 3-body terms of these two complexes is relatively small, constituting only 1/6 of the difference in total interaction energy. The more strongly bound H_2O trimer thus must mainly benefit from its 2-body terms. While the magnitude of ΔE_{12} ($HOH\cdots OH_2$) is only marginally different in these two complexes, the $HOH\cdots{}^{\bullet}OH$ interaction (ΔE_{23}) in $^{\bullet}OH(H_2O)_2$ is markedly weaker than its counterpart in the H_2O trimer (by 1.34 kcal/mol). The $^{\bullet}OH\cdots OH_2$ interaction (ΔE_{13}), on the other hand, is ∼0.9 kcal/mol more favorable than its counterpart in the H_2O trimer, which is however insufficient to compensate for the deficiency in ΔE_{23}. Note that the relative strength of the 2-body interactions in these two complexes are well correlated with the $O\cdots H$ distances for the H-bonds shown in Fig. 11.

The energy components of ΔE_{13} and ΔE_{23} indicate that the H_2O trimer possesses more favorable 1−3 and 2−3 FRZ interactions, which seem to be the main contributor to its stronger overall interaction energy. However, they arise from rather different reasons. The stronger 1−3 H-bond in $^{\bullet}OH\cdots OH_2$ is mainly driven by POL and CT. As a result, the $^{\bullet}OH\cdots O$ distance is 0.07 Å shorter than its counterpart in the H_2O trimer, giving rise to a PAULI term that is ∼3 kcal/mol stronger (see Table S5 in the SI) and consequently a less

favorable FRZ term for the 1−3 H-bond in the radical ternary complex. The more favorable FRZ interaction between fragments 2 and 3 in the H_2O trimer, in contrast, contributes to the stronger $HOH\cdots OH_2$ H-bond than $HOH\cdots{}^{\bullet}OH$: the more repulsive PAULI term of the former is fully compensated by the gains in its ELEC and DISP terms (see Table S5 in the SI), which differs from the case of the 1−3 H-bond where the increase in PAULI overpowers. Combined with substantially more attractive POL and CT terms, the more favorable 2-body interaction between 2 and 3 (ΔE_{23}) turns out to be the dominant reason for the higher stability of the H_2O trimer than that of ${}^{\bullet}OH(H_2O)_2$.

In summary, the strength of the three 2-body interactions is more balanced in the H_2O trimer. Replacing one water molecule with an ${}^{\bullet}OH$ radical strengthens one H-bond (${}^{\bullet}OH\cdots OH_2$) while weakening the other ($HOH\cdots{}^{\bullet}OH$), leading to a less stable ternary complex as the latter effect is more pronounced. The strengthening of the 1−3 H-bond is mainly driven by the enhanced POL and CT when ${}^{\bullet}OH$ serves as the H-donor, while the weakening of the 2−3 H-bond results from the diminished strength of ELEC, DISP, POL, and CT, namely, all attractive forces when ${}^{\bullet}OH$ is in place of H_2O as the H-acceptor. These effects are also fairly local, as indicated by the relatively small difference in the 3-body terms of these two complexes.

5.2 Reaction of ${}^{\bullet}OH$ with Aldehydes

The gas-phase reactions between formaldehyde (HCHO) and acetaldehyde (CH_3CHO) with the ${}^{\bullet}OH$ radical are known to be the main channels for these carbonyl compounds to participate in atmospheric reactions. Using electronic structure calculations, Alvarez-Idaboy et al. characterized stationary points along the ${}^{\bullet}OH$ + HCHO and ${}^{\bullet}OH$ + CH_3CHO reaction pathways.[1] In both reactions ${}^{\bullet}OH$ forms highly stabilized pre-reactive complexes with the aldehyde, which plays an essential role in the reaction mechanism. Meanwhile, for the hydrogen abstraction pathway (where ${}^{\bullet}OH$ attacks the H attached to the carbonyl group),

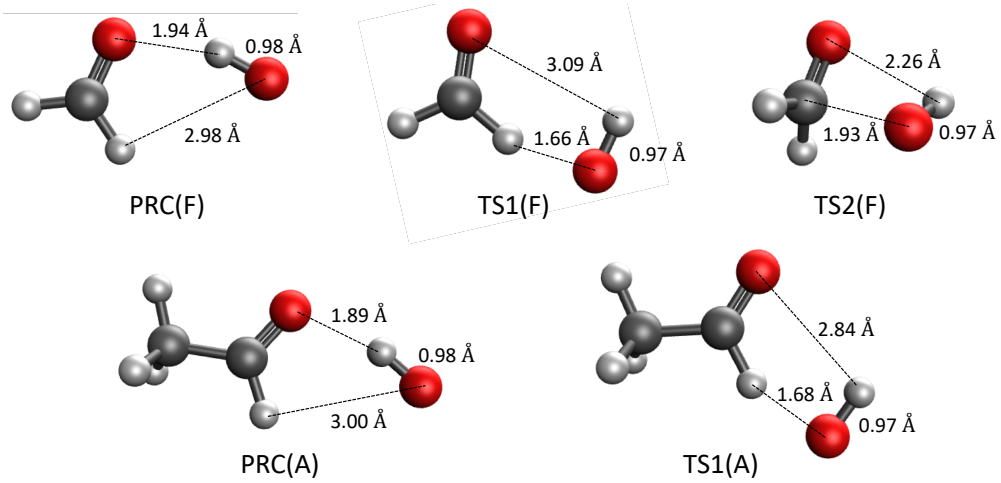

Figure 12: Optimized geometries for the pre-reactive complexes and transition states along the $^{\bullet}$OH + HCHO/CH_3CHO reaction pathways. Top row: the pre-reactive complex (PRC) for $^{\bullet}$OH + HCHO and the transition states for the hydrogen abstraction (TS1) and nucleophilic addition (TS2) reactions; bottom row: the PRC formed by $^{\bullet}$OH and CH_3CHO and the transition state for the hydrogen abstraction (TS1) reaction. "F" and "A" in the parentheses are abbreviations for formaldehyde and acetaldehyde, respectively.

the apparent activation energy (energy difference between TS and non-interacting reactants) is close to zero for HCHO and even more negative for CH_3CHO, while for an alternative nucleophilic attack in which $^{\bullet}$OH adds to the carbonyl group, the barrier was found to be much higher, indicating that this pathway can be excluded.[1]

Using the ωB97M-V/def2-TZVPD model chemistry, we optimized the structures for the critical points in these two reactions, including the pre-reactive complexes (PRCs) formed by $^{\bullet}$OH with each aldehyde and the transition states for their H-abstraction reactions (TS1). As in ref. 1, we also included the TS of the nucleophilic addition pathway for the $^{\bullet}$OH + HCHO reaction (TS2(F)). All these optimized structures are exhibited in Fig. 12, where both PRC(F, A) and TS1(F, A) are planar (C_s symmetry). The unpaired electron is mainly localized on the $^{\bullet}$OH moiety but becomes more delocalized in the TS structures, which is illustrated with the HCHO complexes in Fig. S4 in the SI. We note that the most favorable electronic configuration for the PRCs possesses $^2A''$ symmetry, that is, the unpaired electron is perpendicular to the molecular plane (Fig. S4(a)). In the TS structure for H-abstraction,

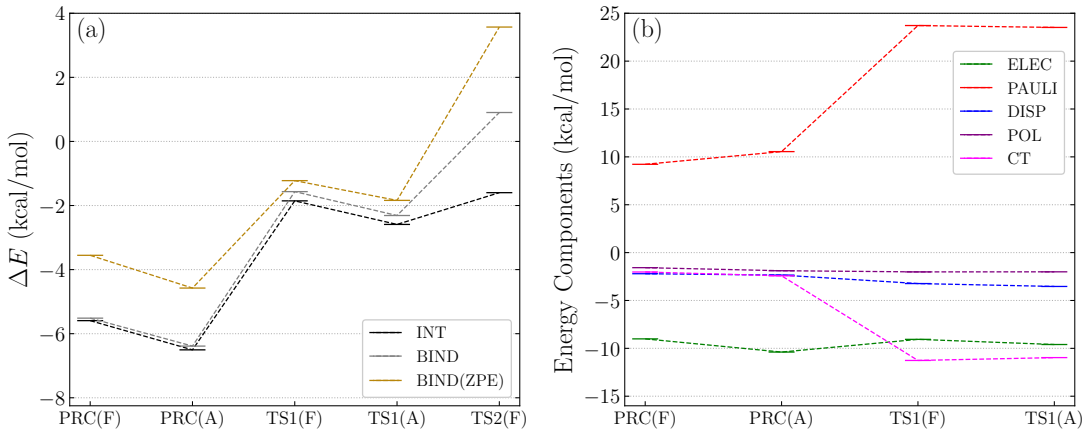

Figure 13: Relative energies (a) and ALMO-EDA results (b) for the stationary geometries characterized in Fig. 12. The left panel shows the interaction energy (INT), binding energy (BIND = INT + GD), and harmonic zero-point energy corrected binding energy (BIND(ZPE)) for each pre-reactive or transition state complexe; the right panel shows the components of the interaction energy for each complex except TS2(F) since its energy components are of a vastly different range (see Table S7 in the SI for its EDA results). Note that the dashed lines connecting energy levels belonging to the same category are only for guiding the eye rather than indicating the reaction pathway.

on the other hand, the $^2A'$ state turns out to be more stable, and the unpaired electron lies in the molecular plane facilitating its attack on the H atom (Fig. S4(c)). This differs from the assignment by Alvarez-Idaboy et al. that both the PRC and TS are of $^2A'$ symmetry.[1] To confirm our results, we further computed the energy difference between $^2A''$ and $^2A'$ for the two PRCs with the M06-2X functional and the model chemistry employed in ref. 1 (MP2/6-311++G(d,p)[102,103]), and the results agree with those given by ωB97M-V (see Table S6 in the SI). Therefore, we use results calculated for the more stable $^2A''$ state for the PRCs; and note again, due to the existence of two closely lying electronic states, the PtD approach combined with wavefunction stability analysis is essential for ensuring the consistency of state symmetry throughout the EDA procedure.

Figure 13(a) depicts the energy landscape for the PRC and TS structures in the $^\bullet$OH + HCHO and $^\bullet$OH + CH_3CHO reactions. The two PRCs are both strongly bound by over 5 kcal/mol, and the one with acetaldehyde (A) is more stable than that with formaldehyde (F)

by ∼1 kcal/mol, indicating that the H-bond between •OH and the carbonyl group is stronger in PRC(A). This is confirmed by PRC(A)'s shorter O$\cdots$H distance (see Fig. 12) and its more favorable ELEC, POL, and CT components as shown in Fig. 13(b), which as a by-product also induces slightly stronger Pauli repulsion. The stronger H-bonding interaction in PRC(A) can be rationalized through the electron-donating effect of the methyl group, which increases the electron density on the carbonyl group and renders the O atom more negative. The effect of zero-point energy (ZPE) destabilizes these two PRCs to approximately the same extent, rendering their relative stability unchanged.

The relative stability of the two transition states for H-abstraction, TS1(F) and TS1(A), is similar to that of the two PRCs, with TS1(A) being more strongly bound by ∼1 kcal/mol. Note that the ZPE-corrected effective activation energies obtained in the present work are too negative compared to the values reported by Alvarez-Idaboy et al.,[1] which were computed at the CCSD(T)/6-311++G(d,p) // MP2/6-311++G(d,p) level of theory. Nevertheless, fairly good agreement is achieved for the energy difference between TS1(F) and TS1(A). These two transition structures feature close contact between •OH and the H atom that is being abstracted, which can be viewed as extraordinarily short H-bonds. The EDA results for these two TS structures (Fig. 13(b)) reveal that CT plays the most significant role in stabilizing these TS complexes, followed by the also substantial ELEC and less pronounced DISP and POL contributions, which differs from the more typical stable H-bonding interactions in the PRCs that are dominated by ELEC. Interestingly, the relative strength of POL and CT in TS1(F) and TS1(A) manifests an opposite trend to their relative strength of binding, suggesting that TS1(F) gains its higher stability mainly through the components of FRZ interaction. Indeed, according to the EDA results, TS1(A) possesses not only more favorable ELEC and DISP interactions compared to those in TS1(F) but also a less repulsive PAULI term, which, taken together, stabilize TS1(A) relative to TS1(F) by over 1 kcal/mol.

The transition state for the nucleophilic addition of •OH to formaldehyde, TS2(F), is

of a rather distinct structure compared to others in Fig. 12, where the O atom in $^{\bullet}$OH is almost exactly above the C atom (the O$\cdots$C=O angle is 92°) and the HCHO molecule is bent slightly (with a dihedral of 8.4°). The interaction between $^{\bullet}$OH and HCHO remains attractive in this complex and is merely 0.25 kcal/mol less favorable compared to that in the TS1(F). The EDA results (see Table S7 in the SI) suggest that ELEC and CT make almost equal contributions to the stabilization of this TS complex, and the strength of POL and DISP is also more than twice as large as those in TS1(F). Nonetheless, as indicated in Fig. 12(a), TS2(F) is subjected to substantial destabilizing effects from GD and ZPE, which results in a much higher effective activation energy (3.6 kcal/mol) and consequently renders the nucleophilic addition pathway unfavorable relative to H-abstraction for the $^{\bullet}$OH + HCHO reaction.

6 Conclusions

In the present work, we demonstrated how the special electronic structure of open-shell species poses a challenge to energy decomposition analysis (EDA) methods employed to probe intermolecular interactions involving radicals. To address this challenge, we have introduced extensions to the absolutely localized molecular orbital (ALMO)-EDA to enable its usage with unrestricted Kohn-Sham density functional theory (KS-DFT) calculations on radical-molecule complexes. Our main conclusions are as follows:

1. The frozen orbital supersystem used in the ALMO-EDA (and other EDAs such as SAPT that also construct this state from isolated fragment MOs) often does not have a uniquely defined energy when the isolated radical has partly occupied degenerate orbitals. We introduced the "polarize-then-depolarize" (PtD) approach to uniquely define the variationally best frozen energy, utilizing intermolecular polarization to resolve the degeneracy of radical's electronic states. This approach was demonstrated

on two model complexes ($H_2O\cdots F^{\bullet}$ and $FH\cdots{}^{\bullet}OH$) that otherwise suffer from the problem of non-unique EDA results.

2. Polarization in radical-neutral complexes arises not only from mixing of singly and doubly occupied levels with strictly empty levels on each fragment, but also from mixing of the doubly occupied orbitals with the singly occupied levels to rehybridize the latter. A procedure to evaluate this REHYB energy as a special contributor to polarization in unrestricted KS-DFT methods is introduced.

3. Since radical-molecule complexes often have more than one low-lying state, one needs to be cautious to consistently follow the desired state through each intermediate (frozen, polarized, unconstrained) state of the EDA. This is facilitated by gradient optimization of polarized and unconstrained states and performing stability analysis on the converged states to ensure a local minimum with respect to orbital rotations.

4. Integrating the above methods with the previously established vertical[42] and adiabatic[46] ALMO-EDA schemes defines a second generation unrestricted ALMO-EDA (uALMO-EDA) approach. The vertical EDA yields useful insights regarding the strength of each energy component, while the adiabatic EDA describes how each component induces changes in observable properties, such as geometry and vibrational frequencies.

5. For the sandwich and T-shaped benzene dimer radical cations, we demonstrated that uALMO-EDA, when paired with state-of-the-art density functionals, is capable of yielding more accurate total interaction energies than SAPT0(UHF). Comparison against the EDA results for the closed-shell dimer isomers reveals that the strengthened binding between two benzene moieties upon ionization arises from enhanced CT, POL, and long-range ELEC as well as diminished Pauli repulsion.

6. Analysis of complexes between pyridine (Py) and the benzene (Bz) and naphthalene (Naph) radical cations ($Bz^{+\bullet}$−Py and $Naph^{+\bullet}$−Py) illustrates how the adiabatic EDA can provide a deeply insightful complement to the vertical EDA. The adiabatic EDA emphasizes the dominant role of CT in the stability of the complexes, and identifies it as the cause of the stronger binding between $Bz^{+\bullet}$ and Py. By contrast, the latter identifies POL as the most substantial binding force and attributes the difference in their total binding energies to the PAULI term. A stronger REHYB term accounts for the larger POL contribution in $Naph^{+\bullet}$−Py (within the vertical uALMO-EDA).

7. We investigated binary and ternary $^{\bullet}$OH–water complexes. The adiabatic uALMO-EDA results for the minimum-energy electronic configuration of $^{\bullet}OH(H_2O)$ reveal that elongation of the $^{\bullet}$O−H bond and red shift in its stretching frequency almost entirely result from CT, akin to the H-bond of the water dimer. These molecular property shifts are almost doubled in the ternary complex, $^{\bullet}OH(H_2O)_2$, with which we demonstrated the application of ALMO-EDA to the many-body expansion (MBE) of the total interaction energy. The MBE shows that the relative stability of $^{\bullet}OH(H_2O)_2$ vs. the H_2O trimer is determined by changes in the strength of the two 2-body interactions.

8. We investigated the pre-reactive complexes (PRC) and transition state complexes in the $^{\bullet}$OH + HCHO and $^{\bullet}$OH + CH_3CHO reactions. $^{\bullet}$OH forms strongly bound PRCs with formaldehyde and acetaldehyde via H-bonds with the carbonyl group ($^{\bullet}OH\cdots O{=}C$), which are governed by attractive electrostatic interactions. In contrast, the TSs for H-abstraction exhibit much shorter $C{-}H\cdots{}^{\bullet}OH$ hydrogen bonds, and CT is the largest stabilizing contribution complexes followed by attractive ELEC.

9. These application examples, taken together, illustrate ways in which uALMO-EDA can facilitate understanding of radical-molecule interactions and thereby assist in the study of radical chemistry in general.

A Approach to quantify the energy lowering associated with the localization of β-hole

Consider an open-shell fragment A with converged unrestricted orbitals $\{\phi_1^\alpha \cdots \phi_{n_\alpha}^\alpha \cdots \phi_{n_A}^\alpha\} \cup \{\phi_1^\beta \cdots \phi_{n_\beta}^\beta \cdots \phi_{n_A}^\beta\}$, where n_α and n_β denote the number of α and β electrons, respectively, and n_A denotes the total number AO basis functions on A. Without losing generality, we also assume $n_\alpha > n_\beta$ for this fragment. Our goal is to define the orbital rotation degrees of freedom that resemble the DS rotations in ROSCF. In most general cases, the orbitals of different spins obtained from a USCF calculation are not properly paired as in the RO case, that is, the ith α and β orbitals can possess entirely different characters. This is illustrated through the left panels of Fig. S5 in the SI using the example of the $H_2O\cdots F^\bullet$ complex. Therefore, it is desirable to find a transformation that aligns the α and β orbitals without varying the USCF energy of this fragment. Here we adopt Löwdin's orbital pairing scheme that were originally employed to correspond MOs from two determinants that are nonorthogonal to each other.[104] Defining $\mathbf{C}_{\mathrm{o},\alpha}$ and $\mathbf{C}_{\mathrm{o},\beta}$ as the MO coefficient matrices for the occupied α and β orbitals, we first form the overlap between them

$$\mathbf{S}_{\mathrm{oo}}^{\alpha\beta} = \mathbf{C}_{\mathrm{o},\alpha}^T \mathbf{S}_A \mathbf{C}_{\mathrm{o},\beta} \tag{A.1}$$

and then singular-value decompose (SVD) it

$$\mathbf{S}_{\mathrm{oo}}^{\alpha\beta} = \mathbf{U}_\alpha \mathbf{s} \mathbf{V}_\beta^T \tag{A.2}$$

where the $\mathbf{S}_A$ matrix in Eq. (A.1) is the overlap matrix of AO basis functions on fragment A. Using the left and right singular vectors from the SVD, one can obtain the Löwdin-paired

orbitals by rotating the original α and β occupied orbitals

$$\mathbf{C}'_{\mathrm{o},\alpha} = \mathbf{C}_{\mathrm{o},\alpha}\mathbf{U}_\alpha \tag{A.3}$$

$$\mathbf{C}'_{\mathrm{o},\beta} = \mathbf{C}_{\mathrm{o},\beta}\mathbf{V}_\beta \tag{A.4}$$

With the occupied α and β MOs aligned, we still need to rotate the virtual orbitals in the β space to make the lowest-lying $n_\alpha - n_\beta$ ones resemble the singly occupied orbitals in RO. We first partition the rotated α MOs into a doubly-like ("d") and a singly-like ("s") group, that is, $\mathbf{C}'_{\mathrm{o},\alpha} \equiv [\mathbf{C}'_{\mathrm{d},\alpha}, \mathbf{C}'_{\mathrm{s},\alpha}]$, where $\mathbf{C}'_{\mathrm{d},\alpha}$ stands for the first n_α columns of $\mathbf{C}'_{\mathrm{o},\alpha}$ and $\mathbf{C}'_{\mathrm{s},\alpha}$ for the rest $n_\alpha - n_\beta$ columns. Then we form the overlap between $\mathbf{C}'_{\mathrm{s},\alpha}$ and all β virtual orbitals ($\mathbf{C}'_{\mathrm{v},\beta}$)

$$\mathbf{S}^{\alpha\beta}_{\mathrm{sv}} = (\mathbf{C}'_{\mathrm{s},\alpha})^T \mathbf{S}_A \mathbf{C}'_{\mathrm{v},\beta} \tag{A.5}$$

and perform another SVD

$$\mathbf{S}^{\alpha\beta}_{\mathrm{sv}} = \mathbf{U}'_\alpha \mathbf{s}' (\mathbf{V}'_\beta)^T \tag{A.6}$$

Denoting the first $n_\alpha - n_\beta$ columns of $\mathbf{V}'_\beta$ as $\mathbf{V}'_{\mathrm{s},\beta}$, the following transformation yields the β virtuals that resemble the singly-like α orbitals ($\mathbf{C}'_{\mathrm{s},\alpha}$) the most, which are denoted as $\mathbf{C}'_{\mathrm{s},\beta}$

$$\mathbf{C}'_{\mathrm{s},\beta} = \mathbf{C}'_{\mathrm{v},\beta}\mathbf{V}'_{\mathrm{s},\beta} \tag{A.7}$$

and correspondingly the singly-like α orbitals are rotated one more time

$$\mathbf{C}''_{\mathrm{s},\alpha} = \mathbf{C}'_{\mathrm{s},\alpha}\mathbf{U}'_\alpha \tag{A.8}$$

The resulting paired α and β orbitals whose MO coefficients are represented by $[\mathbf{C}'_{\mathrm{d},\alpha}, \mathbf{C}''_{\mathrm{s},\alpha}]$ and $[\mathbf{C}'_{\mathrm{o},\beta}, \mathbf{C}'_{\mathrm{s},\beta}]$, respectively, are shown in the right panels of Fig. S5 in the SI. In the special SCF-MI calculation for the rehybridization step that we mentioned in Sec. 4, we only allow

orbital mixings between the doubly-like and singly-like orbitals in fragment A's β space with all other orbital rotation degrees of freedom frozen. The variational subspaces for this special SCF-MI problem can thus be denoted as $[\mathbf{C}'^{A}_{\mathrm{o},\beta}, \mathbf{C}'^{A}_{\mathrm{s},\beta}]@[\mathbf{C}'^{A}_{\mathrm{d},\alpha}, \mathbf{C}''^{A}_{\mathrm{s},\alpha}] \oplus \bigcup_{I}^{N_F-1}[\mathbf{C}^{I}_{\mathrm{o},\alpha}, \mathbf{C}^{I}_{\mathrm{o},\beta}]$, where the orbitals on the right-hand side of "@", including the α occupied orbitals on A and both the α and β occupied orbitals on other fragments, remain unchanged in this SCF-MI calculation and serve as the environment that the active β orbitals on fragment A are embedded in. In our code implementation, such an SCF-MI calculation is enabled by simply deleting those frozen degrees of freedom from the full orbital gradient vector in the GDM[86] optimization of the SCF-MI energy. The energy lowering associated with this special SCF-MI calculation relative to the energy of the frozen state is defined as the rehybridization energy ($\Delta E_{\mathrm{REHYB}}$), which describes the stabilization effect arising from the electron density reorganization on the open-shell fragment that localizes its β-hole in the presence of other fragments:

$$\Delta E_{\mathrm{REHYB}} = E^{\mathrm{DS}}_{\text{SCF-MI}} - E_{\mathrm{FRZ}} \tag{A.9}$$

where $E^{\mathrm{DS}}_{\text{SCF-MI}}$ stands for the energy of the supersystem at the convergence of the above-described SCF-MI calculation that permits DS-like orbital rotations only.

Acknowledgement

This work was supported by the U.S. National Science Foundation Grant No. CHE-1665315 and CHE-1955643, with additional support from CALSOLV. Y.M. thanks Xiaotian Qi from University of Pittsburgh and Colin K. Egan from University of California, San Diego for providing valuable feedback on the program implementation and other practical aspects of this method.

References

(1) Alvarez-Idaboy, J. R.; Mora-Diez, N.; Boyd, R. J.; Vivier-Bunge, A. On the importance of prereactive complexes in molecule-radical reactions: hydrogen abstraction from aldehydes by OH. *J. Am. Chem. Soc.* **2001**, *123*, 2018–2024.

(2) Hansen, J. C.; Francisco, J. S. Radical–Molecule Complexes: Changing Our Perspective on the Molecular Mechanisms of Radical–Molecule Reactions and their Impact on Atmospheric Chemistry. *ChemPhysChem* **2002**, *3*, 833–840.

(3) Smith, I. W.; Ravishankara, A. Role of hydrogen-bonded intermediates in the bimolecular reactions of the hydroxyl radical. *J. Phys. Chem. A* **2002**, *106*, 4798–4807.

(4) Church, J. R.; Vaida, V.; Skodje, R. T. Gas-Phase Reaction Kinetics of Pyruvic Acid with OH Radicals: The Role of Tunneling, Complex Formation, and Conformational Structure. *J. Phys. Chem. A* **2020**, *124*, 790–800.

(5) Vöhringer-Martinez, E.; Hansmann, B.; Hernandez, H.; Francisco, J.; Troe, J.; Abel, B. Water catalysis of a radical-molecule gas-phase reaction. *Science* **2007**, *315*, 497–501.

(6) Long, B.; Zhang, W.-J.; Tan, X.-F.; Long, Z.-W.; Wang, Y.-B.; Ren, D.-S. Theoretical study on the gas phase reaction of sulfuric acid with hydroxyl radical in the presence of water. *J. Phys. Chem. A* **2011**, *115*, 1350–1357.

(7) Vaida, V. Perspective: Water cluster mediated atmospheric chemistry. *J. Chem. Phys.* **2011**, *135*, 020901.

(8) Gonzalez, J.; Anglada, J. M.; Buszek, R. J.; Francisco, J. S. Impact of water on the OH+ HOCl reaction. *J. Am. Chem. Soc.* **2011**, *133*, 3345–3353.

(9) Buszek, R. J.; Francisco, J. S.; Anglada, J. M. Water effects on atmospheric reactions. *Int. Rev. Phys. Chem.* **2011**, *30*, 335–369.

(10) Zhang, T.; Wang, W.; Li, C.; Du, Y.; Lü, J. Catalytic effect of a single water molecule on the atmospheric reaction of HO_2 + OH: fact or fiction? A mechanistic and kinetic study. *RSC Adv.* **2013**, *3*, 7381–7391.

(11) Chao, W.; Yin, C.; Takahashi, K.; Lin, J. J.-M. Hydrogen-Bonding Mediated Reactions of Criegee Intermediates in the Gas Phase: Competition between Bimolecular and Termolecular Reactions and the Catalytic Role of Water. *J. Phys. Chem. A* **2019**, *123*, 8336–8348.

(12) Attah, I. K.; Platt, S. P.; Meot-Ner, M.; El-Shall, M. S.; Peverati, R.; Head-Gordon, M. What is the structure of the naphthalene–benzene heterodimer radical cation? Binding energy, charge delocalization, and unexpected charge-transfer interaction in stacked dimer and trimer radical cations. *J. Phys. Chem. Lett.* **2015**, *6*, 1111–1118.

(13) Peverati, R.; Platt, S. P.; Attah, I. K.; Aziz, S. G.; El-Shall, M. S.; Head-Gordon, M. Nucleophilic Aromatic Addition in Ionizing Environments: Observation and Analysis of New C–N Valence Bonds in Complexes between Naphthalene Radical Cation and Pyridine. *J. Am. Chem. Soc.* **2017**, *139*, 11923–11932.

(14) Bera, P. P.; Stein, T.; Head-Gordon, M.; Lee, T. J. Mechanisms of the formation of adenine, guanine, and their analogues in UV-irradiated mixed NH3: H2O molecular ices containing purine. *Astrobiology* **2017**, *17*, 771–785.

(15) Xu, B.; Stein, T.; Ablikim, U.; Jiang, L.; Hendrix, J.; Head-Gordon, M.; Ahmed, M. Probing solvation and reactivity in ionized polycyclic aromatic hydrocarbon–water clusters with photoionization mass spectrometry and electronic structure calculations. *Faraday Discuss.* **2019**, *217*, 414–433.

(16) Clark, T. Interaction of Radicals with σ-Holes. *J. Phys. Chem. A* **2019**, *123*, 3326–3333.

(17) Bandyopadhyay, P.; Ray, S.; Seikh, M. M. Unraveling the regioselectivity of odd electron halogen bond formation using electrophilicity index and chemical hardness parameters. *Phys. Chem. Chem. Phys.* **2019**, *21*, 26580–26590.

(18) Xie, Y.; Schaefer III, H. F. Hydrogen bonding between the water molecule and the hydroxyl radical (H_2O·HO): The global minimum. *J. Chem. Phys.* **1993**, *98*, 8829–8834.

(19) Du, S.; Francisco, J. S.; Schenter, G. K.; Iordanov, T. D.; Garrett, B. C.; Dupuis, M.; Li, J. The OH radical–H_2O molecular interaction potential. *J. Chem. Phys.* **2006**, *124*, 224318.

(20) Ang, S. J.; Mak, A. M.; Wong, M. W. Nature of halogen bonding involving π-systems, nitroxide radicals and carbenes: a highlight of the importance of charge transfer. *Phys. Chem. Chem. Phys.* **2018**, *20*, 26463–26478.

(21) Altun, A.; Saitow, M.; Neese, F.; Bistoni, G. Local Energy Decomposition of Open-Shell Molecular Systems in the Domain-Based Local Pair Natural Orbital Coupled Cluster Framework. *J. Chem. Theory Comput.* **2019**, *15*, 1616–1632.

(22) Phipps, M. J.; Fox, T.; Tautermann, C. S.; Skylaris, C.-K. Energy decomposition analysis approaches and their evaluation on prototypical protein–drug interaction patterns. *Chem. Soc. Rev.* **2015**, *44*, 3177–3211.

(23) Pastorczak, E.; Corminboeuf, C. Perspective: Found in translation: Quantum chemical tools for grasping non-covalent interactions. *J. Chem. Phys.* **2017**, *146*, 120901.

(24) Zhao, L.; von Hopffgarten, M.; Andrada, D. M.; Frenking, G. Energy decomposition analysis. *WIREs: Comput. Mol. Sci.* **2018**, *8*, e1345.

(25) Neese, F.; Atanasov, M.; Bistoni, G.; Maganas, D.; Ye, S. Chemistry and quantum mechanics in 2019: Give us insight and numbers. *J. Am. Chem. Soc.* **2019**, *141*, 2814–2824.

(26) Jeziorski, B.; Moszynski, R.; Szalewicz, K. Perturbation theory approach to intermolecular potential energy surfaces of van der Waals complexes. *Chem. Rev.* **1994**, *94*, 1887–1930.

(27) Parker, T. M.; Burns, L. A.; Parrish, R. M.; Ryno, A. G.; Sherrill, C. D. Levels of symmetry adapted perturbation theory (SAPT). I. Efficiency and performance for interaction energies. *J. Chem. Phys.* **2014**, *140*, 094106.

(28) Żuchowski, P. S.; Podeszwa, R.; Moszyński, R.; Jeziorski, B.; Szalewicz, K. Symmetry-adapted perturbation theory utilizing density functional description of monomers for high-spin open-shell complexes. *J. Chem. Phys.* **2008**, *129*, 084101.

(29) Hapka, M.; Żuchowski, P. S.; Szcześniak, M. M.; Chałasiński, G. Symmetry-adapted perturbation theory based on unrestricted Kohn-Sham orbitals for high-spin open-shell van der Waals complexes. *J. Chem. Phys.* **2012**, *137*, 164104.

(30) Gonthier, J. F.; Sherrill, C. D. Density-fitted open-shell symmetry-adapted perturbation theory and application to π-stacking in benzene dimer cation and ionized DNA base pair steps. *J .Chem. Phys.* **2016**, *145*, 134106.

(31) Green, M. C.; Fedorov, D. G.; Kitaura, K.; Francisco, J. S.; Slipchenko, L. V. Open-shell pair interaction energy decomposition analysis (PIEDA): Formulation and application to the hydrogen abstraction in tripeptides. *J. Chem. Phys.* **2013**, *138*, 074111.

(32) Marjolin, A.; Gourlaouen, C.; Clavaguéra, C.; Dognon, J.-P.; Piquemal, J.-P. Towards energy decomposition analysis for open and closed shell f-elements mono aqua complexes. *Chem. Phys. Lett.* **2013**, *563*, 25–29.

(33) Lein, M.; Szabó, A.; Kovács, A.; Frenking, G. Energy decomposition analysis of the chemical bond in main group and transition metal compounds. *Faraday Discuss.* **2003**, *124*, 365–378.

(34) Su, P.; Li, H. Energy decomposition analysis of covalent bonds and intermolecular interactions. *J. Chem. Phys.* **2009**, *131*, 014102.

(35) Horn, P. R.; Sundstrom, E. J.; Baker, T. A.; Head-Gordon, M. Unrestricted absolutely localized molecular orbitals for energy decomposition analysis: Theory and applications to intermolecular interactions involving radicals. *J. Chem. Phys.* **2013**, *138*, 134119.

(36) Wu, Q. Variational nature of the frozen density energy in density-based energy decomposition analysis and its application to torsional potentials. *J. Chem. Phys.* **2014**, *140*, 244109.

(37) Tang, Z.; Jiang, Z.; Chen, H.; Su, P.; Wu, W. Energy decomposition analysis based on broken symmetry unrestricted density functional theory. *J. Chem. Phys.* **2019**, *151*, 244106.

(38) Neese, F. Importance of direct spin- spin coupling and spin-flip excitations for the zero-field splittings of transition metal complexes: a case study. *J. Am. Chem. Soc.* **2006**, *128*, 10213–10222.

(39) Knowles, P. J.; Andrews, J. S.; Amos, R. D.; Handy, N. C.; Pople, J. A. Restricted Møller—Plesset theory for open-shell molecules. *Chem. Phys. Lett.* **1991**, *186*, 130–136.

(40) Loipersberger, M.; Lee, J.; Mao, Y.; Das, A. K.; Ikeda, K.; Thirman, J.; Head-Gordon, T.; Head-Gordon, M. Energy Decomposition Analysis for Interactions of Radicals: Theory and Implementation at the MP2 Level with Application to Hydration of Halogenated Benzene Cations and Complexes between $CO_2^{-\bullet}$ and Pyridine and Imidazole. *J. Phys. Chem. A* **2019**, *123*, 9621–9633.

(41) Khaliullin, R. Z.; Cobar, E. A.; Lochan, R. C.; Bell, A. T.; Head-Gordon, M. Unravelling the origin of intermolecular interactions using absolutely localized molecular orbitals. *J. Phys. Chem. A* **2007**, *111*, 8753–8765.

(42) Horn, P. R.; Mao, Y.; Head-Gordon, M. Probing non-covalent interactions with a second generation energy decomposition analysis using absolutely localized molecular orbitals. *Phys. Chem. Chem. Phys.* **2016**, *18*, 23067–23079.

(43) Horn, P. R.; Head-Gordon, M. Polarization contributions to intermolecular interactions revisited with fragment electric-field response functions. *J. Chem. Phys.* **2015**, *143*, 114111.

(44) Horn, P. R.; Mao, Y.; Head-Gordon, M. Defining the contributions of permanent electrostatics, Pauli repulsion, and dispersion in density functional theory calculations of intermolecular interaction energies. *J. Chem. Phys.* **2016**, *144*, 114107.

(45) Mao, Y.; Demerdash, O.; Head-Gordon, M.; Head-Gordon, T. Assessing ion-water interactions in the AMOEBA force field using energy decomposition analysis of electronic structure calculations. *J. Chem. Theory Comput.* **2016**, *12*, 5422–5437.

(46) Mao, Y.; Horn, P. R.; Head-Gordon, M. Energy decomposition analysis in an adiabatic picture. *Phys. Chem. Chem. Phys.* **2017**, *19*, 5944–5958.

(47) Ramos-Cordoba, E.; Lambrecht, D. S.; Head-Gordon, M. Charge-transfer and the

hydrogen bond: Spectroscopic and structural implications from electronic structure calculations. *Faraday Discuss.* **2011**, *150*, 345–362.

(48) Mao, Y.; Head-Gordon, M. Probing Blue-Shifting Hydrogen Bonds with Adiabatic Energy Decomposition Analysis. *J. Phys. Chem. Lett.* **2019**, *10*, 3899–3905.

(49) Thirman, J.; Engelage, E.; Huber, S. M.; Head-Gordon, M. Characterizing the interplay of Pauli repulsion, electrostatics, dispersion and charge transfer in halogen bonding with energy decomposition analysis. *Phys. Chem. Chem. Phys.* **2018**, *20*, 905–915.

(50) Mao, Y.; Ge, Q.; Horn, P. R.; Head-Gordon, M. On the Computational Characterization of Charge-Transfer Effects in Noncovalently Bound Molecular Complexes. *J. Chem. Theory Comput.* **2018**, *14*, 2401–2417.

(51) Rossomme, E. C.; Lininger, C. N.; Bell, A. T.; Head-Gordon, T.; Head-Gordon, M. Electronic structure calculations permit identification of the driving forces behind frequency shifts in transition metal monocarbonyls. *Phys. Chem. Chem. Phys.* **2020**, *22*, 781–798.

(52) Loipersberger, M.; Mao, Y.; Head-Gordon, M. Variational Forward-Backward Charge Transfer Analysis Based on Absolutely Localized Molecular Orbitals: Energetics and Molecular Properties. *J. Chem. Theory Comput.* **2020**, *16*, 1073–1089.

(53) Levine, D. S.; Horn, P. R.; Mao, Y.; Head-Gordon, M. Variational energy decomposition analysis of chemical bonding. 1. Spin-pure analysis of single bonds. *J. Chem. Theory Comput.* **2016**, *12*, 4812–4820.

(54) Levine, D. S.; Head-Gordon, M. Energy decomposition analysis of single bonds within Kohn–Sham density functional theory. *Proc. Natl. Acad. Sci. U.S.A* **2017**, *114*, 12649–12656.

(55) Ge, Q.; Mao, Y.; Head-Gordon, M. Energy decomposition analysis for exciplexes using absolutely localized molecular orbitals. *J. Chem. Phys.* **2018**, *148*, 064105.

(56) Ge, Q.; Head-Gordon, M. Energy decomposition analysis for excimers using absolutely localized molecular orbitals within time-dependent density functional theory and configuration interaction with single excitations. *J. Chem. Theory Comput.* **2018**, *14*, 5156–5168.

(57) Thirman, J.; Head-Gordon, M. An energy decomposition analysis for second-order Møller–Plesset perturbation theory based on absolutely localized molecular orbitals. *J. Chem. Phys.* **2015**, *143*, 084124.

(58) Thirman, J.; Head-Gordon, M. Efficient Implementation of Energy Decomposition Analysis for Second-Order Møller–Plesset Perturbation Theory and Application to Anion–π Interactions. *J. Phys. Chem. A* **2017**, *121*, 717–728.

(59) Mitoraj, M. P.; Michalak, A.; Ziegler, T. A Combined Charge and Energy Decomposition Scheme for Bond Analysis. *J. Chem. Theory Comput.* **2009**, *5*, 962–975.

(60) von Hopffgarten, M.; Frenking, G. Energy decomposition analysis. *WIREs Comput. Mol. Sci.* **2012**, *2*, 43–62.

(61) Mo, Y.; Gao, J.; Peyerimhoff, S. D. Energy decomposition analysis of intermolecular interactions using a block-localized wave function approach. *J. Chem. Phys.* **2000**, *112*, 5530–5538.

(62) Mo, Y.; Song, L.; Lin, Y. Block-localized wavefunction (BLW) method at the density functional theory (DFT) level. *J. Phys. Chem. A* **2007**, *111*, 8291–8301.

(63) Mo, Y.; Bao, P.; Gao, J. Energy decomposition analysis based on a block-localized

wavefunction and multistate density functional theory. *Phys. Chem. Chem. Phys.* **2011**, *13*, 6760–6775.

(64) Tentscher, P. R.; Arey, J. S. Binding in radical-solvent binary complexes: Benchmark energies and performance of approximate methods. *J. Chem. Theory Comput.* **2013**, *9*, 1568–1579.

(65) Kohn, W.; Sham, L. J. Self-consistent equations including exchange and correlation effects. *Phys. Rev.* **1965**, *140*, A1133.

(66) Pople, J. A.; Gill, P. M.; Johnson, B. G. Kohn–Sham density-functional theory within a finite basis set. *Chem. Phys. Lett.* **1992**, *199*, 557–560.

(67) Stoll, H.; Wagenblast, G.; Preuß, H. On the Use of Local Basis Sets for Localized Molecular Orbitals. *Theor. Chem. Acc.* **1980**, *57*, 169–178.

(68) Gianinetti, E.; Raimondi, M.; Tornaghi, E. Modification of the Roothaan Equations to Exclude BSSE from Molecular Interaction Calculations. *Int. J. Quantum Chem.* **1996**, *60*, 157–166.

(69) Khaliullin, R. Z.; Head-Gordon, M.; Bell, A. T. An efficient self-consistent field method for large systems of weakly interacting components. *J. Chem. Phys.* **2006**, *124*, 204105.

(70) Azar, R. J.; Horn, P. R.; Sundstrom, E. J.; Head-Gordon, M. Useful lower limits to polarization contributions to intermolecular interactions using a minimal basis of localized orthogonal orbitals: Theory and analysis of the water dimer. *J. Chem. Phys.* **2013**, *138*, 084102.

(71) Lao, K. U.; Herbert, J. M. Energy Decomposition Analysis with a Stable Charge-Transfer Term for Interpreting Intermolecular Interactions. *J. Chem. Theory Comput.* **2016**, *12*, 2569–2582.

(72) Gilbert, A. T.; Besley, N. A.; Gill, P. M. Self-consistent field calculations of excited states using the maximum overlap method (MOM). *J. Phys. Chem. A* **2008**, *112*, 13164–13171.

(73) Barca, G. M.; Gilbert, A. T.; Gill, P. M. Simple models for difficult electronic excitations. *J. Chem. Theory Comput.* **2018**, *14*, 1501–1509.

(74) Pulay, P. Improved SCF convergence acceleration. *J. Comput. Chem.* **1982**, *3*, 556–560.

(75) Levine, D. S.; Head-Gordon, M. Quantifying the role of orbital contraction in chemical bonding. *J. Phys. Chem. Lett.* **2017**, *8*, 1967–1972.

(76) Shao, Y.; Gan, Z.; Epifanovsky, E.; Gilbert, A. T.; Wormit, M.; Kussmann, J.; Lange, A. W.; Behn, A.; Deng, J.; Feng, X.; Ghosh, D.; Goldey, M.; Horn, P. R.; Jacobson, L. D.; Kaliman, I.; Khaliullin, R. Z.; Kuś, T.; Landau, A.; Liu, J.; Proynov, E. I.; Rhee, Y. M.; Richard, R. M.; Rohrdanz, M. A.; Steele, R. P.; Sundstrom, E. J.; Woodcock, H. L.; Zimmerman, P. M.; Zuev, D.; Albrecht, B.; Alguire, E.; Austin, B.; Beran, G. J. O.; Bernard, Y. A.; Berquist, E.; Brandhorst, K.; Bravaya, K. B.; Brown, S. T.; Casanova, D.; Chang, C.-M.; Chen, Y.; Chien, S. H.; Closser, K. D.; Crittenden, D. L.; Diedenhofen, M.; DiStasio, R. A.; Do, H.; Dutoi, A. D.; Edgar, R. G.; Fatehi, S.; Fusti-Molnar, L.; Ghysels, A.; Golubeva-Zadorozhnaya, A.; Gomes, J.; Hanson-Heine, M. W.; Harbach, P. H.; Hauser, A. W.; Hohenstein, E. G.; Holden, Z. C.; Jagau, T.-C.; Ji, H.; Kaduk, B.; Khistyaev, K.; Kim, J.; Kim, J.; King, R. A.; Klunzinger, P.; Kosenkov, D.; Kowalczyk, T.; Krauter, C. M.; Lao, K. U.; Laurent, A.; Lawler, K. V.; Levchenko, S. V.; Lin, C. Y.; Liu, F.; Livshits, E.; Lochan, R. C.; Luenser, A.; Manohar, P.; Manzer, S. F.; Mao, S.-P.; Mardirossian, N.; Marenich, A. V.; Maurer, S. A.; Mayhall, N. J.; Neuscamman, E.;

Oana, C. M.; Olivares-Amaya, R.; O'Neill, D. P.; Parkhill, J. A.; Perrine, T. M.; Peverati, R.; Prociuk, A.; Rehn, D. R.; Rosta, E.; Russ, N. J.; Sharada, S. M.; Sharma, S.; Small, D. W.; Sodt, A.; Stein, T.; Stück, D.; Su, Y.-C.; Thom, A. J.; Tsuchimochi, T.; Vanovschi, V.; Vogt, L.; Vydrov, O.; Wang, T.; Watson, M. A.; Wenzel, J.; White, A.; Williams, C. F.; Yang, J.; Yeganeh, S.; Yost, S. R.; You, Z.-Q.; Zhang, I. Y.; Zhang, X.; Zhao, Y.; Brooks, B. R.; Chan, G. K.; Chipman, D. M.; Cramer, C. J.; Goddard, W. A.; Gordon, M. S.; Hehre, W. J.; Klamt, A.; Schaefer, H. F.; Schmidt, M. W.; Sherrill, C. D.; Truhlar, D. G.; Warshel, A.; Xu, X.; Aspuru-Guzik, A.; Baer, R.; Bell, A. T.; Besley, N. A.; Chai, J.-D.; Dreuw, A.; Dunietz, B. D.; Furlani, T. R.; Gwaltney, S. R.; Hsu, C.-P.; Jung, Y.; Kong, J.; Lambrecht, D. S.; Liang, W.; Ochsenfeld, C.; Rassolov, V. A.; Slipchenko, L. V.; Subotnik, J. E.; Van Voorhis, T.; Herbert, J. M.; Krylov, A. I.; Gill, P. M.; Head-Gordon, M. Advances in molecular quantum chemistry contained in the Q-Chem 4 program package. *Mol. Phys.* **2015**, *113*, 184–215.

(77) Mardirossian, N.; Head-Gordon, M. ωB97M-V: A combinatorially optimized, range-separated hybrid, meta-GGA density functional with VV10 nonlocal correlation. *J. Chem. Phys.* **2016**, *144*, 214110.

(78) Weigend, F.; Ahlrichs, R. Balanced basis sets of split valence, triple zeta valence and quadruple zeta valence quality for H to Rn: Design and assessment of accuracy. *Phys. Chem. Chem. Phys.* **2005**, *7*, 3297–3305.

(79) Rappoport, D.; Furche, F. Property-optimized Gaussian basis sets for molecular response calculations. *J. Chem. Phys.* **2010**, *133*, 134105.

(80) Vydrov, O. A.; Van Voorhis, T. Nonlocal van der Waals density functional: The simpler the better. *J. Chem. Phys.* **2010**, *133*, 244103.

(81) Mardirossian, N.; Head-Gordon, M. Thirty years of density functional theory in computational chemistry: an overview and extensive assessment of 200 density functionals. *Mol. Phys.* **2017**, *115*, 2315–2372.

(82) Manna, D.; Kesharwani, M. K.; Sylvetsky, N.; Martin, J. M. Conventional and explicitly correlated ab initio benchmark study on water clusters: revision of the BEGDB and WATER27 datasets. *J. Chem. Theory Comput.* **2017**, 3136–3152.

(83) Zhao, Y.; Truhlar, D. G. The M06 suite of density functionals for main group thermochemistry, thermochemical kinetics, noncovalent interactions, excited states, and transition elements: two new functionals and systematic testing of four M06-class functionals and 12 other functionals. *Theor. Chem. Acc.* **2008**, *120*, 215–241.

(84) Gill, P. M.; Johnson, B. G.; Pople, J. A. A standard grid for density functional calculations. *Chem. Phys. Lett.* **1993**, *209*, 506–512.

(85) Handy, N. C.; Schaefer III, H. F. On the evaluation of analytic energy derivatives for correlated wave functions. *J. Chem. Phys.* **1984**, *81*, 5031–5033.

(86) Van Voorhis, T.; Head-Gordon, M. A geometric approach to direct minimization. *Mol. Phys.* **2002**, *100*, 1713–1721.

(87) Sosa, C.; Geertsen, J.; Trucks, G. W.; Bartlett, R. J.; Franz, J. A. Selection of the reduced virtual space for correlated calculations. An application to the energy and dipole moment of H2O. *Chem. Phys. Lett.* **1989**, *159*, 148–154.

(88) Taube, A. G.; Bartlett, R. J. Frozen natural orbital coupled-cluster theory: Forces and application to decomposition of nitroethane. *J. Chem. Phys.* **2008**, *128*, 164101.

(89) Landau, A.; Khistyaev, K.; Dolgikh, S.; Krylov, A. I. Frozen natural orbitals for

ionized states within equation-of-motion coupled-cluster formalism. *J. Chem. Phys,* **2010**, *132*, 014109.

(90) Mao, Y.; Shao, Y.; Dziedzic, J.; Skylaris, C.-K.; Head-Gordon, T.; Head-Gordon, M. Performance of the AMOEBA water model in the vicinity of QM solutes: A diagnosis using energy decomposition analysis. *J. Chem. Theory Comput.* **2017**, *13*, 1963–1979.

(91) Mardirossian, N.; Head-Gordon, M. ωB97X-V: A 10-parameter, range-separated hybrid, generalized gradient approximation density functional with nonlocal correlation, designed by a survival-of-the-fittest strategy. *Phys. Chem. Chem. Phys.* **2014**, *16*, 9904–9924.

(92) Dunning Jr, T. H. Gaussian basis sets for use in correlated molecular calculations. I. The atoms boron through neon and hydrogen. *J. Chem. Phys.* **1989**, *90*, 1007–1023.

(93) Jensen, F. Polarization consistent basis sets: principles. *J. Chem. Phys.* **2001**, *115*, 9113–9125.

(94) Jensen, F. Polarization consistent basis sets. II. Estimating the Kohn–Sham basis set limit. *J. Chem. Phys.* **2002**, *116*, 7372–7379.

(95) Monks, P. S. Gas-phase radical chemistry in the troposphere. *Chem. Soc. Rev.* **2005**, *34*, 376–395.

(96) Atkinson, R.; Arey, J. Atmospheric degradation of volatile organic compounds. *Chem. Rev.* **2003**, *103*, 4605–4638.

(97) Mellouki, A.; Le Bras, G.; Sidebottom, H. Kinetics and mechanisms of the oxidation of oxygenated organic compounds in the gas phase. *Chem. Rev.* **2003**, *103*, 5077–5096.

(98) Hernandez, F. J.; Brice, J. T.; Leavitt, C. M.; Liang, T.; Raston, P. L.; Pino, G. A.; Douberly, G. E. Mid-infrared signatures of hydroxyl containing water clusters: Infrared

laser Stark spectroscopy of OH–H2O and $OH(D_2O)_n$ (n = 1–3). *J. Chem. Phys.* **2015**, *143*, 164304.

(99) Allodi, M. A.; Dunn, M. E.; Livada, J.; Kirschner, K. N.; Shields, G. C. Do hydroxyl radical–water clusters, $OH(H_2O)_n$, n = 1–5, exist in the atmosphere? *J. Phys. Chem. A* **2006**, *110*, 13283–13289.

(100) Ohshima, Y.; Sato, K.; Sumiyoshi, Y.; Endo, Y. Rotational Spectrum and Hydrogen Bonding of the H2O–HO Radical Complex. *J. Am. Chem. Soc.* **2005**, *127*, 1108–1109.

(101) Li, X.; Liu, L.; Schlegel, H. B. On the physical origin of blue-shifted hydrogen bonds. *J. Am. Chem. Soc.* **2002**, *124*, 9639–9647.

(102) Krishnan, R.; Binkley, J. S.; Seeger, R.; Pople, J. A. Self-consistent molecular orbital methods. XX. A basis set for correlated wave functions. *J. Chem. Phys.* **1980**, *72*, 650–654.

(103) Frisch, M. J.; Pople, J. A.; Binkley, J. S. Self-consistent molecular orbital methods 25. Supplementary functions for Gaussian basis sets. *J. Chem. Phys.* **1984**, *80*, 3265–3269.

(104) Löwdin, P.-O. On the non-orthogonality problem connected with the use of atomic wave functions in the theory of molecules and crystals. *J. Chem. Phys.* **1950**, *18*, 365–375.

Graphical TOC Entry